JOURNAL OF PETROLOGY

Journal of Petrology, 2018, Vol. 59, No. 10, 1991–2016
doi: 10.1093/petrology/egy087
Advance Access Publication Date: 7 September 2018
Original Article

OXFORD

Textural and Mineralogical Record of Low-pressure Melt Extraction and Silicic Cumulate Formation in the Late Miocene Risco Bayo–Huemul Plutonic Complex, Southern Andes

Allen J. Schaen [1]*, Brad S. Singer[1], John M. Cottle[2], Nicolas Garibaldi[1], Blair Schoene[3], Aaron M. Satkoski[1] and John Fournelle[1]

[1]Department of Geoscience, University of Wisconsin–Madison, Madison, WI 53706, USA; [2]Department of Earth Science, University of California, Santa Barbara, CA 93106, USA; [3]Department of Geosciences, Princeton University, Princeton, NJ 08544, USA

*Corresponding author. E-mail: schaen@wisc.edu

Received March 3, 2018; Accepted August 30, 2018

ABSTRACT

One model for rhyolite generation in the upper crust is via extraction of interstitial melt from crystal-rich magma reservoirs. Although silicic magma reservoirs may grow incrementally over *c.* 10^4–10^5 yr timescales, they can be remobilized prior to eruption much more rapidly (*c.* 10^1–10^3 yr). This process implies the formation of cumulate residues with a composition complementary to the extracted melt, but the predicted cumulates have so far eluded widespread identification. The 7·2–6·2 Ma Risco Bayo–Huemul plutonic complex comprises ~150 km^3 that is subdivided into at least seven gabbroic to granitic domains emplaced at <7 km depth. Distinct Ti, Zr, Nb, and rare earth element variations in amphibole document pulsed emplacement of the gabbroic to granodioritic Risco Bayo pluton ~800 kyr prior to the adjacent quartz monzonite to high-silica granite of the Huemul pluton. The quartz monzonite is inferred to be a silicic cumulate on the basis of whole-rock mass balance and enrichments in Ba and Zr concentrations. Here, we combine fine-scale textural analysis using energy-dispersive X-ray spectrometry (EDS) phase mapping with *in situ* mineral compositions to explore the silicic cumulate hypothesis. Quartz monzonite textures are porphyritic and comprise ~58–64 modal % of partially interlocking, 2–5 mm long euhedral plagioclase, together with euhedral biotite, orthoclase, and amphibole. The finer-grained interstitial matrix is composed of anhedral orthoclase, plagioclase, and quartz. Calculations using the compositions of the interstitial phases suggest that the matrix represents a highly evolved melt similar in major and trace element chemistry to coeval, high-silica granite inferred to be extracted and frozen rhyolite. The high-silica granites are equigranular and contain dense concentrations of miarolitic cavities implying, together with Al-in-Hbl barometry for the quartz monzonite, emplacement and volatile saturation within the upper crust at the granite minimum. Plagioclase, orthoclase, and biotite in high-silica granite are depleted in Ba, Sr, and Eu, similar to their bulk-rock compositions, and support an origin as highly fractionated products of melt extraction. Miarolitic cavities within the high-silica granite overlying the granite domain suggest that volatiles played an important role in the upward percolation of melt. Our observations indicating transport of volatiles and melt through an underlying crystal mush, including accumulation of vapor bubbles at the roof of the magma

reservoir, are consistent with recent numerical simulations of multi-phase fluid dynamics within compositionally zoned silicic reservoirs that feed large explosive eruptions.

Key words: silicic cumulate; granite; melt extraction; anti-rapakivi; Andes

INTRODUCTION

The relationship between plutonic and volcanic rocks remains controversial, despite decades of study (e.g. Johnson *et al.*, 1989; Bachmann & Huber, 2016; Lundstrom & Glazner, 2016, and references therein). Part of the debate revolves around the depths and processes leading up to the generation of silicic (>74 wt % SiO_2) rock compositions (i.e. high-silica granite and rhyolite). The combination of observations from many perspectives (e.g. petrology, geochemistry, geochronology, geophysics, thermal modelling) has led to different hypotheses regarding how and where magmas differentiate within the crust, with lower crustal partial melting and upper crustal *in situ* fractional crystallization being two end-member models (e.g. Bowen, 1928; Daly, 1933; Wager *et al.*, 1960; Hildreth, 1981; Petford *et al.*, 2000; Miller & Miller, 2002; Coleman *et al.*, 2004; Glazner *et al.*, 2004; Annen *et al.*, 2006; Bachmann *et al.*, 2007; Michel *et al.*, 2008; Singer *et al.*, 2014).

Contamination, fractionation, and hybridization of mantle melts within the lower crust has long been recognized as an important process in continental arc settings [i.e. the MASH (melting–assimilation–storage–homogenization) zone of Hildreth & Moorbath (1988)]. One perspective is that differentiation within these lower crustal MASH zones is primarily responsible for the geochemical diversity seen in the upper crust (e.g. Coleman *et al.*, 2004; Glazner *et al.*, 2004; Annen *et al.*, 2006). These models suggest that magmas are transported from the lower crust by discrete dikes briefly transiting the middle to upper crust, and thus large-volume super-eruptions represent a snapshot of magma emplaced or erupted quickly during periods of high magma flux (e.g. Tappa *et al.*, 2011; Schöpa & Annen, 2013). In this sense, a batholith that is heterogeneous in its composition or lithology is the amalgamation of separate pulses of magma that did not interact as liquids at the site of emplacement (e.g. Coleman *et al.*, 2004, 2012; Tappa *et al.*, 2011). According to this model, volcanic reservoirs do not leave behind residual magma as plutons, precluding a genetic link between plutonic and volcanic systems (e.g. Glazner *et al.*, 2008; Mills & Coleman, 2013).

Although acknowledging the fundamental role for lower crustal processes, an alternative perspective is that MASH zone signatures can be overprinted by *in situ* crystal–liquid separation within the middle to upper crust (<10 km depth; e.g. Bachmann & Bergantz, 2004, 2008; Hildreth, 2004; Bachmann *et al.*, 2005, 2007). This view considers some plutonic rocks as representative of the residual material left behind after volcanic eruptions (e.g. Lipman, 2007; Gelman *et al.*, 2014; Lipman & Bachmann, 2015; Deering *et al.*, 2016). The shallow reservoirs that contain melt in the upper crust are thought to comprise extensive crystal-rich mush zones (~45–70% crystals) that may contain interconnected melt and domains of crystal-poor melt that occasionally erupt (e.g. Hildreth, 2004; Bachmann & Bergantz, 2008; Miller *et al.*, 2011). One version of the mush model posits that upper crustal magma reservoirs can remain in almost fully crystalline states for 10^4–10^5 yr prior to rapid reactivation and eruption (e.g. Cooper & Kent, 2014; Andersen *et al.*, 2017; Rubin *et al.*, 2017). Phase equilibria constrain the low-pressure origin of high-silica compositions (e.g. Gualda & Ghiorso, 2013) and imply the presence of pluton-sized reservoirs that reside and differentiate within the upper crust (e.g. Hildreth, 2004).

Separation of rhyolitic melt from magma reservoirs implies the concurrent formation of geochemically complementary crystalline residues. However, the predicted geochemical signatures of such residues are not readily identified in the global rock record (Glazner *et al.*, 2015; Keller *et al.*, 2015), which has led some researchers to search for them on the scale of individual plutonic or batholithic systems (e.g. Bachl *et al.*, 2001; Claiborne *et al.*, 2006; Deering & Bachmann, 2010; Lee & Morton, 2015; Fiedrich *et al.*, 2017; Schaen *et al.*, 2017). A challenge to identifying 'silicic cumulate' compositions may be that melt extraction is inefficient within high-viscosity or high-crystallinity magmas, such that some trapped melt freezes within the cumulate (e.g. Deering & Bachmann, 2010; Lee & Morton, 2015). Another challenge confronting widespread identification of rocks that reflect this process is the inherent variability of granitoid textures, which are less readily recognized as cumulates compared with their mafic counterparts.

Schaen *et al.* (2017) used bulk-rock geochemical modelling along with temporal and chemical constraints provided by U–Pb zircon petrochronology to hypothesize that high-silica granites unmixed from complementary silicic cumulates to form the Huemul pluton in Chile. Throughout our study, we use the term 'unmixing' *sensu stricto* in reference to the chemical fractionation effect on a bulk starting composition imparted by the mechanical extraction of high-silica melt and concentration of residual crystals, as described by Schaen *et al.* (2017). We examine the textures and mineral compositions of this system with a specific focus on testing the unmixing hypothesis. Although the Huemul rocks are spatially, temporally, and geochemically closely associated (Schaen *et al.*, 2017), we argue here that they also share a textural relationship that records melt extraction and concomitant

crystal accumulation. We leverage quantitative textural analysis from energy-dispersive spectrometry (EDS) phase mapping and *in situ* major and trace element contents of minerals to test the hypothesis that the silicic cumulate rocks contain remnants of trapped melt left over from the extraction of the high-silica granite.

GEOLOGICAL SETTING

The Late Miocene Risco Bayo–Huemul (RBH) plutonic complex is located within the Southern Volcanic Zone of the Andean Cordillera at 36°S (Fig. 1). The main exposure of the complex sits beneath the northern flank of the Quaternary frontal arc Tatara–San Pedro volcanic complex (Singer *et al.*, 1997; Dungan *et al.*, 2001). The crust here is 40–50 km thick and its surface is 130–150 km above the Wadati–Benioff zone (Hildreth & Moorbath, 1988; Campos *et al.*, 2002; Yuan *et al.*, 2006; Heit *et al.*, 2008).

Plutonic rocks of the Chilean Andes preserve an episodic and migratory record of Paleozoic, Mesozoic, and Oligocene–Late Miocene magmatism distributed in north–south-trending parallel linear belts (Fig. 1; Drake *et al.*, 1982; Parada, 1990). Miocene plutons of the Andean Cordillera intruded a several kilometers thick sequence of folded Mesozoic strata and are commonly roofed by folded Oligocene to Miocene meta-volcanic rocks (Drake, 1976; Drake *et al.*, 1982; Muñoz and Niemeyer, 1984; Kay *et al.*, 2005). Early mapping and K–Ar dating (Drake, 1976; Muñoz and Niemeyer, 1984), followed by additional $^{40}Ar/^{39}Ar$ dating (Nelson *et al.* 1999), revealed several Miocene plutons in the region adjacent to Tatara–San Pedro volcano (35–36°S; Fig. 1). Fifteen kilometers north of the RBH plutonic complex, Drake (1976) K–Ar dated one sample from the Invernada pluton at ~7 Ma (Fig. 1), and using $^{40}Ar/^{39}Ar$ methods Nelson *et al.* (1999) re-dated a sample from the 500 km^2 Melado batholith (15 km NW of the RBH complex) at ~16 Ma, making these four plutons the youngest known intrusions in the region. Older plutonic bodies in this area include the ~100 km^2 El Indio pluton $^{40}Ar/^{39}Ar$ dated at ~80 Ma (Nelson *et al.*, 1999).

FIELD RELATIONS AND PETROGRAPHY

The RBH complex (~150 km^3) is exposed along canyons of the Rio Colorado, where rapid exhumation, and deep Quaternary glaciation, have resulted in ~1200 m of vertical exposure through the roof of the complex (Fig. 2; Singer *et al.*, 1997; Nelson *et al.*, 1999). Both plutons intrude Oligocene to Miocene metavolcanic rocks of the Trapa-Trapa and Cura-Mallin Formations (Muñoz and Niemeyer, 1984). The wall-rock is texturally variable, dark green or gray, fine-grained to porphyritic andesite lava and pyroclastic rock metamorphosed locally to hornfels and incorporated into the plutons as angular centimeter- to meter-sized xenoliths (Fig. 3d). The complex comprises two plutons and can be subdivided into distinct, mappable, magmatic domains (Fig. 2) defined

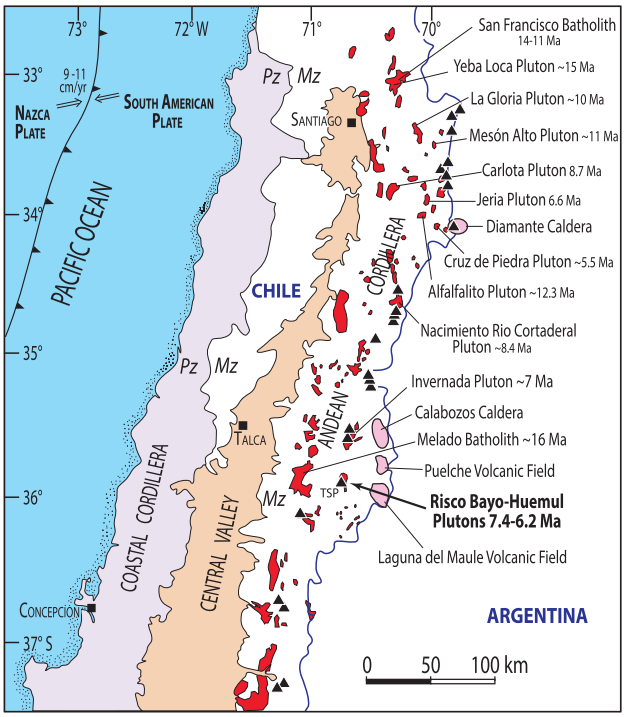

Fig. 1. Schematic regional and tectonic map. Red areas, Paleozoic (Pz) and Mesozoic (Mz) plutons of the Andean cordillera; black triangles, Quaternary SVZ frontal arc; pink areas, calderas or volcanic fields that have produced atypical amounts of silicic eruptive units. Continental divide and Cordilleran range crest is the border between Chile and Argentina, shown by a blue line. TSP, Tatara–San Pedro Volcano. Miocene plutonism age data are from Drake (1976), Drake *et al.* (1982), Muñoz and Niemeyer (1984), Parada (1990), Stern & Skewes (1995), Cornejo & Mahood (1997), Kurtz *et al.* (1997), and Deckart *et al.* (2010). Adapted from Hildreth & Moorbath (1988) and Hildreth *et al.* (2010).

by a combination of lithology, bulk-rock composition, U–Pb zircon age, and zircon trace element composition (Schaen *et al.*, 2017). These domains, which in detail contain some lithological variation typical of granitoids, are used for convenience and encompass observations beyond just rock type (see Table 1 for details).

Risco Bayo pluton

The 7·2–6·4 Ma Risco Bayo (RB) pluton (Schaen *et al.*, 2017) crops out over 25 km^2 and is mafic to intermediate in composition, comprising domains of gabbro, fine-grained diorite, porphyritic diorite and granodiorite, each separated by sharp contacts in the northeastern portion of the pluton (Figs 2 and 3). RB assemblages are dominated by plagioclase, biotite, amphibole, zircon, and apatite with interstitial orthopyroxene and clinopyroxene found in the gabbro and orthoclase in the granodiorite. Quartz is interstitial in most domains apart from the gabbro. Gabbro is observed in small (~0·07 km^2) exposures along the eastern edge of the complex where irregular sharp magmatic contacts separate it from the fine-grained diorite. At this contact, 20–60 cm subrounded blocks of gabbro and angular hornfels wall-rock xenoliths are incorporated into the fine-grained

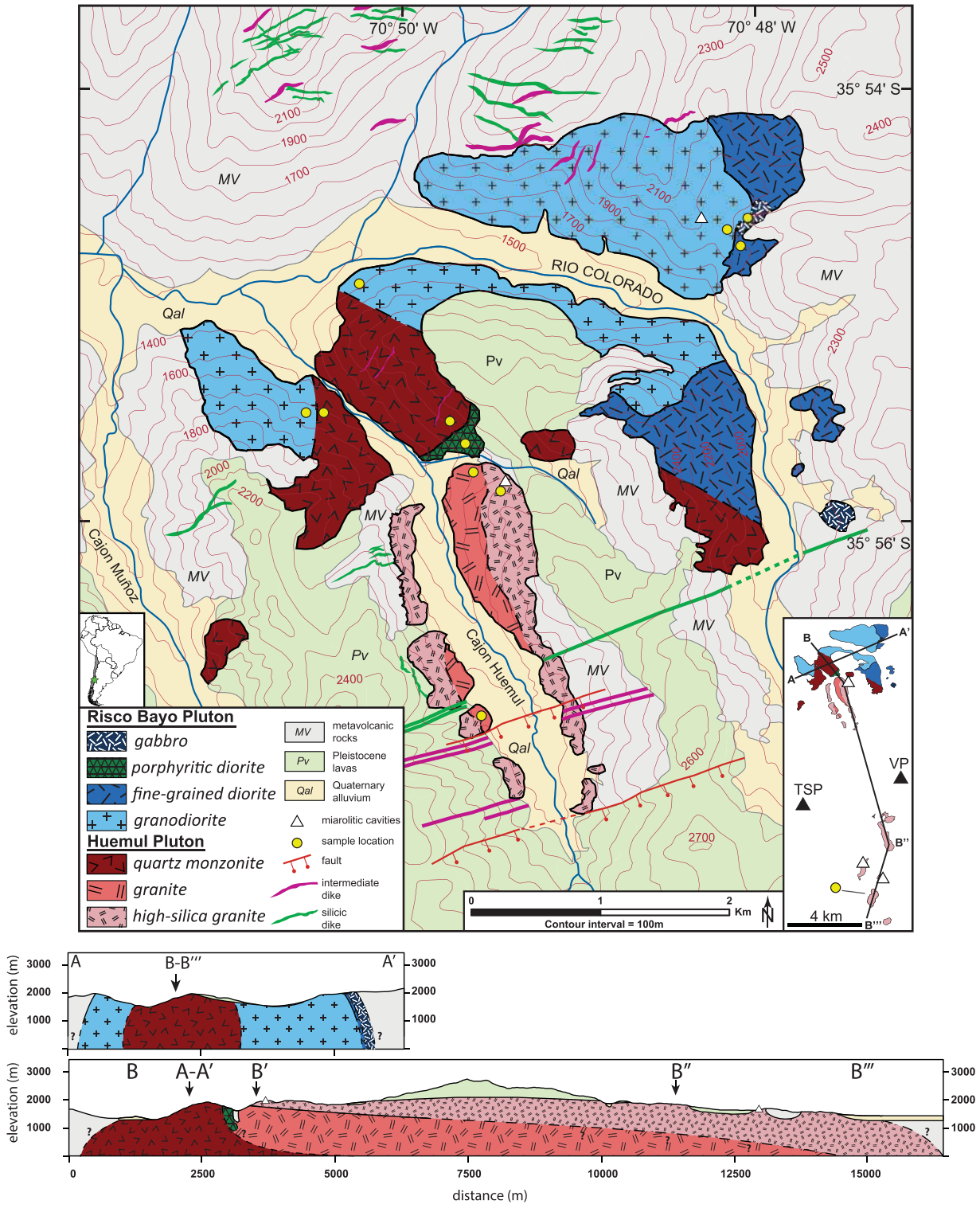

Fig. 2. Map and cross-sections of the Risco Bayo–Huemul plutonic complex, highlighting the compositional domains of this study (modified from Singer *et al.*, 1997; Nelson *et al.*, 1999). Continuous lines indicate sharp contacts; dashed lines are gradational contacts. Elevation in meters. Inset shows the southern extent of the Huemul pluton, the Tatara–San Pedro (TSP) and Pellado (VP) volcanoes, and cross-section lines.

diorite (Fig. 3d). In this same NE region, the fine-grained diorite is in sharp contact with the granodiorite, where both are glacially polished; this sinuous contact is also preserved across the Rio Colorado to the south (Fig. 2). Along this irregular boundary and throughout, 5–20 cm sub-rounded fine-grained enclaves of fine-grained diorite are incorporated into the granodiorite (Fig. 3c). Interfingered dikes, 1–2 m thick, of granodiorite cross-cut the

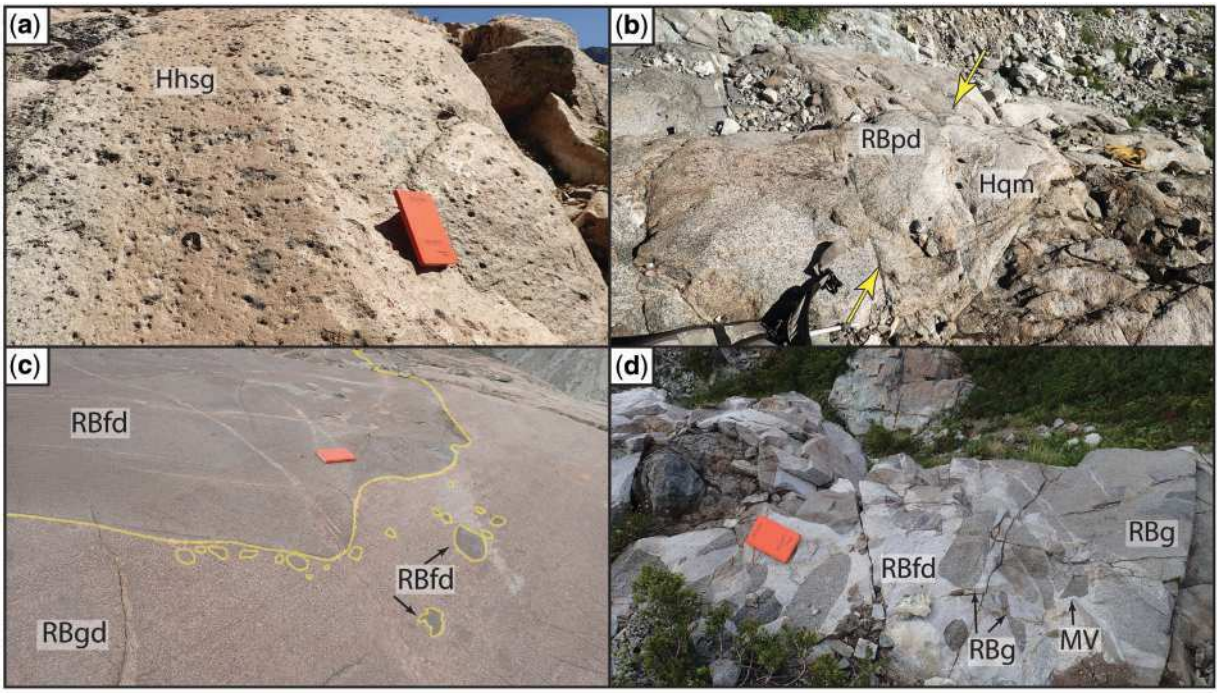

Fig. 3. Field relationships within the Risco Bayo–Huemul plutonic complex. (a) Portion of an ~2000 m^2 zone of miarolitic cavities (~10 vol. % abundance) within the Huemul high-silica granite (Hhsg) domain. (b) Sharp magmatic contact (indicated by arrows) between the Risco Bayo porphyritic diorite (RBpd) and the Huemul quartz monzonite (Hqm) domains. (c) Sharp magmatic contact within Risco Bayo between the fine-grained diorite (RBfd) and granodiorite domains (RBgd). Later felsic veins cross-cut both units. (d) Sharp magmatic contact of the Risco Bayo gabbro (RBg) and metavolcanic wall-rock (MV) inclusions within the fine-grained diorite. Orange field book is 19 cm long.

Table 1: Risco Bayo–Huemul magmatic domains

Pluton	Domain	Abbreviation	Lithologies	SiO_2 (wt %)	U–Pb zircon LA age range (Ma)
Risco Bayo	gabbro	RBg	gabbro	51	~7·2–6·9
Risco Bayo	porphyritic diorite	RBpd	quartz diorite–diorite	57–58	~6·9–6·4
Risco Bayo	fine-grained diorite	RBfd	quartz diorite–diorite	55	~7·2–6·9
Risco Bayo	granodiorite	RBgd	granodiorite–monzogranite	62–66	~7·2–6·9
Huemul	quartz monzonite	Hqm	quartz monzonite–quartz monzodiorite	62–63	~6·4–6·2
Huemul	granite	Hg	monzogranite	68–70	~6·4–6·2
Huemul	high-silica granite	Hhsg	alkali feldspar granite–syenogranite	75–77	~6·4–6·2

gabbro and fine-grained diorite and extend into hornfels wall-rock to the west. These cross-cutting relationships imply a relative sequence of emplacement (from oldest to youngest) of gabbro → fine-grained diorite → granodiorite, although all three record coeval U–Pb zircon crystallization dates of between 7·2 and 6·9 Ma at the ~4% level of precision attainable by laser ablation inductively coupled mass spectrometry (LA-ICP-MS; Schaen *et al.*, 2017). Miarolitic cavities (1–2 vol. %) infilled with tourmaline and epidote are present throughout the granodiorite. Macroscopic field foliations within RB domains are defined by faint to moderate alignment of euhedral to subhedral amphibole (1–3 mm) and biotite (1–4 mm). Field observations paired with thin section analyses, including undeformed euhedral feldspars and lack of quartz recrystallization, reveal that the fabrics are magmatic in origin. Foliation measurements at the contacts between domains and the wall-rock suggest sub-vertical (~70°) emplacement (Fig. 2). The porphyritic diorite is the youngest domain (*c.* 6·9–6·4 Ma) and is texturally (fine grained vs porphyritic) and geochemically different from the fine-grained diorite (Schaen *et al.*, 2017). The porphyritic diorite crops out in an isolated 0·15 km^2 exposure within the Huemul pluton (Fig. 2). A sharp contact separates it from Huemul quartz monzonite where large blocks of fine-grained hornfels wall-rock are included in the porphyritic diorite (Fig. 3b). At the contact with Huemul, foliation in the porphyritic diorite is vertical. At its southeastern contact, the porphyritic diorite is brecciated, hosted in a Huemul granitic matrix, and intermingled with hornfels clasts (10–200 cm).

Huemul pluton

The ~6·4–6·2 Ma Huemul pluton (Schaen *et al.*, 2017) is a north–south elongate body that spans a 5 km × 16 km

region south of the Risco Bayo pluton (Fig. 2). It is felsic and distinguished by three compositional domains including quartz monzonite, granite, and high-silica granite (Fig. 2). Huemul rocks comprise plagioclase, orthoclase, quartz, biotite, amphibole, magnetite, apatite, zircon and titanite (Fig. 4). Amphibole is present in both the quartz monzonite and granite (5–15 modal %), but not in the high-silica granite; biotite is present in each Huemul domain. Titanite occurs in the quartz monzonite and granite and is typically a late-formed phase, but is not seen in the high-silica granite. Roof exposures of the high-silica granite are observed throughout Cajon Huemul, with the granite underlying the high-silica granite at gradational contacts (Fig. 2). This field constraint, along with identical bulk-rock composition and zircon petrochronological signatures, led Schaen *et al.* (2017) to suggest that the high-silica granite is a laterally continuous body spanning ~60 km^2 (including the southernmost outcrops) and sits above the granite domain (Fig. 2). Within an ~2000 m^2 zone the high-silica granite contains ~10 vol. % miarolitic cavities (1–4 cm) infilled with euhedral quartz, orthoclase, tourmaline, and fluorite (Fig. 3a). Aplitic dikes (50–100 cm) cross-cut the high-silica granite and hornfels at contacts with the wall-rock. Mafic enclaves (5–20 cm) are common in the quartz monzonite and granite but not the high-silica granite.

RESULTS

Textures

EDS was used to create phase maps of rocks from each of the Huemul domains to highlight textural relationships and to quantify modal abundances (Fig 5). These were generated by mapping EDS spectra (Si, K, Ca, Na, Al, Ti, Mg, Fe, Zr, P, etc.) over an entire thin section and using the clustering 'AutoPhaseMap' method within the Aztec 3.3 software package (Oxford Instruments; Statham *et al.*, 2013).

All rocks from the quartz monzonite domain share similar porphyritic textures, including 58–64% zoned euhedral plagioclase (2–5 mm) partially interlocking with euhedral biotite (1–3 mm), amphibole (1–3 mm) and orthoclase (3–4 mm; Figs 4 and 5). Plagioclase occurs commonly in apparent synneusis clusters (Vance, 1969) and the euhedral orthoclase exhibits bright back-scattered electron (BSE) cores along with microperthite (Fig. 6). There is a second finer-grained (≤1 mm) anhedral population of plagioclase (unzoned) and orthoclase (no cores) in these rocks, which, along with anhedral quartz (≤1 mm), is interstitial to the euhedral network of crystals (Fig. 5a and c). The interstitial matrix forms 36–42 area % in the quartz monzonite. The proportion of euhedral plagioclase varies somewhat throughout the domain, but this porphyritic texture and clustering of haplogranite mineralogy in the interstices is always preserved. Also found only in the quartz monzonite domain are anti-rapakivi textures: euhedral plagioclase mantled with orthoclase. The anti-rapakivi occurs in two forms, a single plagioclase core mantled by an orthoclase rim or a euhedral plagioclase core with alternating mantles of orthoclase and plagioclase (Fig. 6c, d, and e). Less common sieve textures in plagioclase are also present.

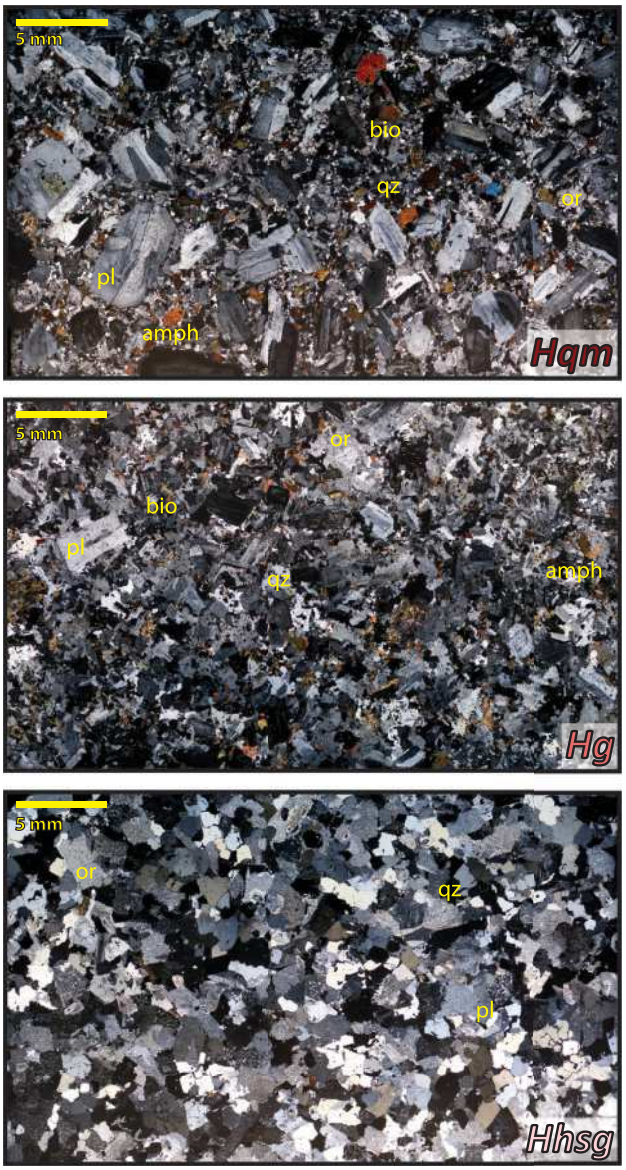

Fig. 4. Crossed-polarized (XPL) full thin section photomicrographs of three domains from the Huemul pluton. These thin sections of quartz monzonite HC1305 (Hqm), granite HC1301 (Hg), and high-silica granite BOTA92 (Hhsg) correlate with the phase maps in Fig. 5. pl, plagioclase; or, orthoclase; qz, quartz; bio, biotite; amph, amphibole.

The textures of the high-silica granite domain are considerably different from those of the quartz monzonite in that all rocks from the high-silica granite are equigranular (Fig. 5e). Orthoclase is euhedral to subhedral, with variable macroperthite textures that take the form of nodular albite lamellae. Plagioclase (oligoclase–albite) is finer (<4 mm) than in the quartz monzonite. Quartz is coarser (1–3 mm) and more abundant, with myrmekitic to micrographic textures found within zones of miarolitic cavities (not shown). The textures found

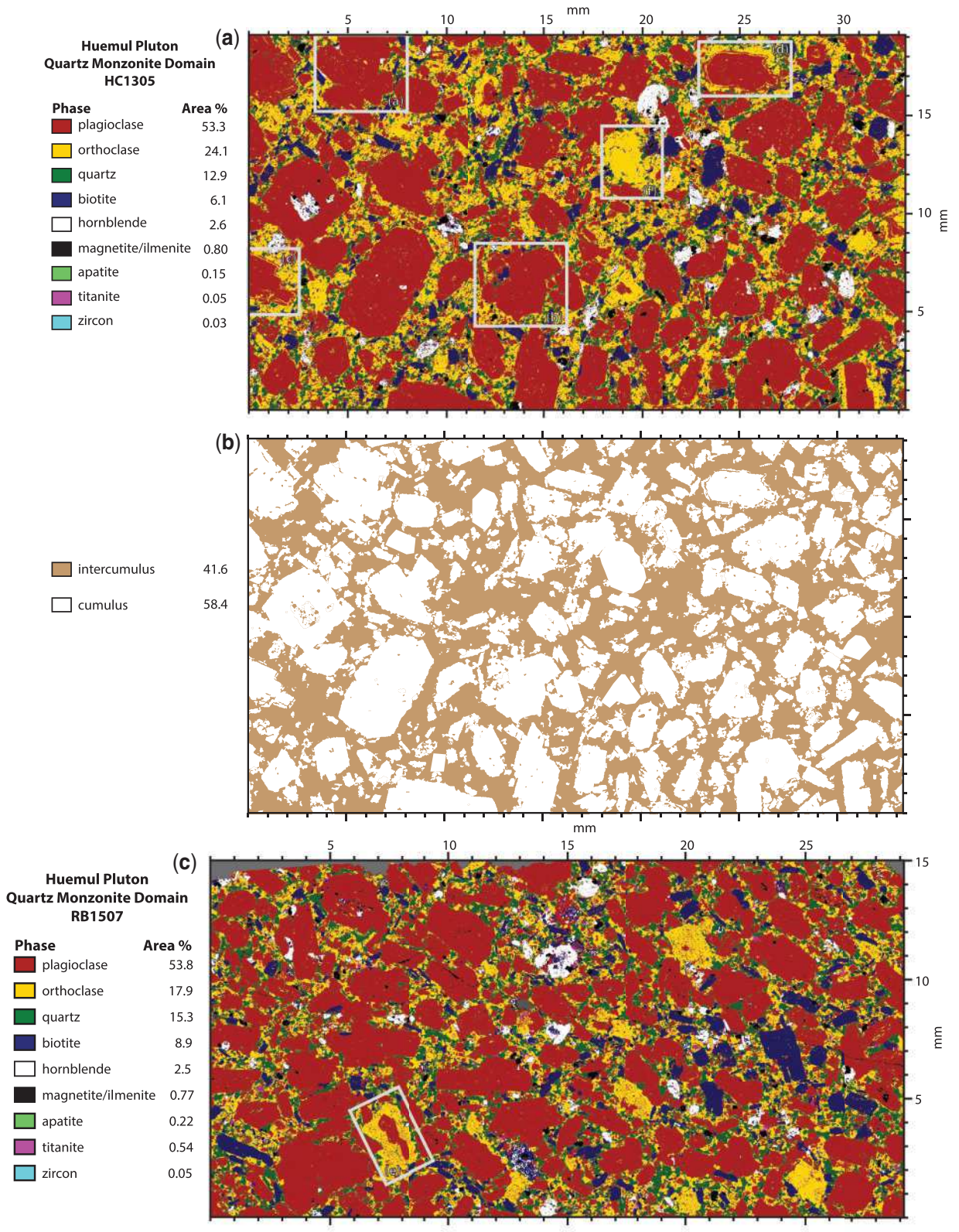

Fig. 5. (a–c) Full thin section energy-dispersive spectrometry (EDS) phase maps from quartz monzonite hand samples: (a) HC1305; (b) distinction between cumulus framework and intercumulus matrix (discussed in the text) in HC1305; (c) RB1507. Highlighted regions (a)–(f) of feldspar textures appear in Fig. 6. Gray regions are unassigned. (d, e) Full thin section energy-dispersive spectrometry (EDS) phase maps of (d) granite and (e) high-silica granite domains within the Huemul pluton. Gray regions are unassigned.

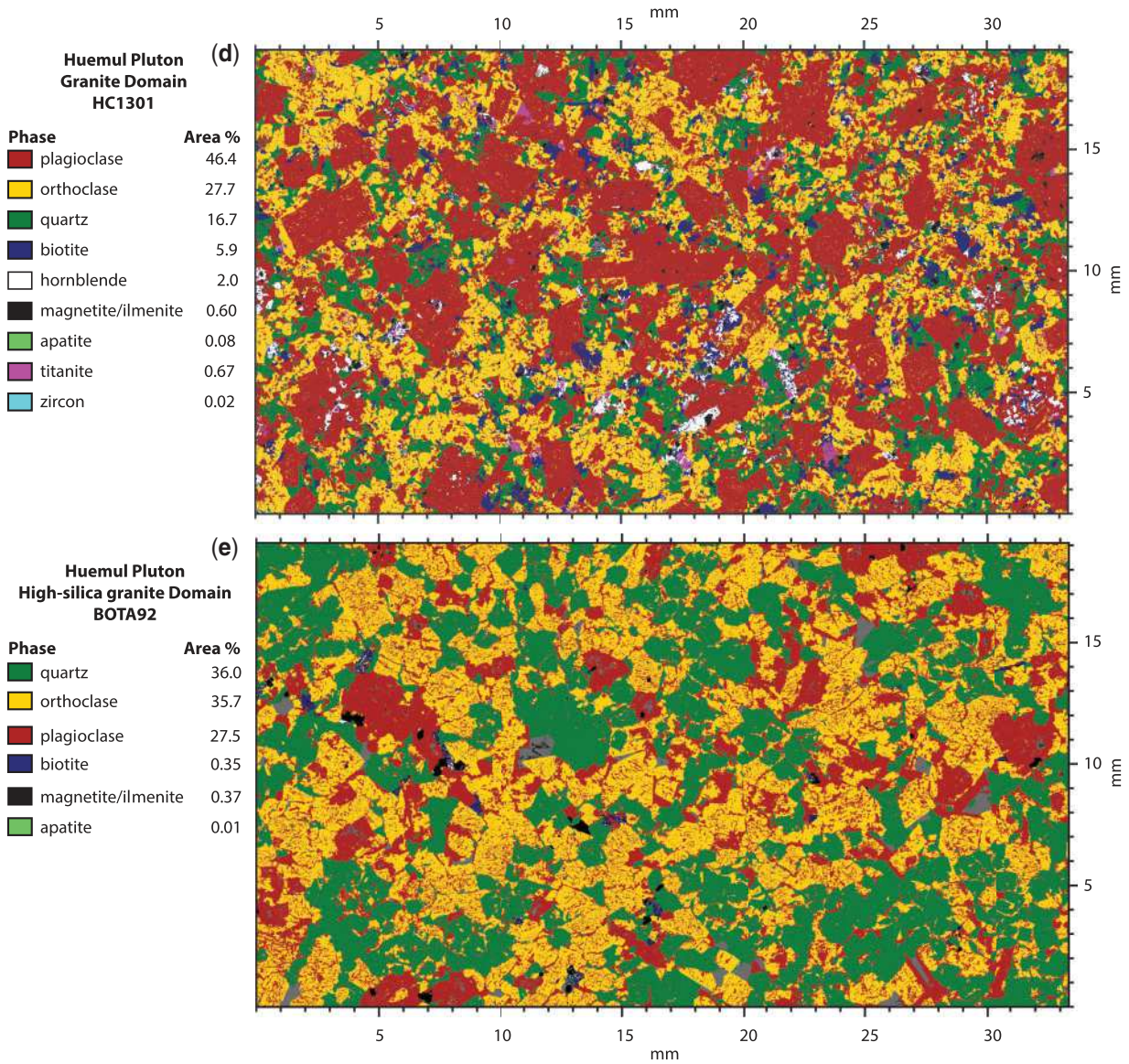

Fig. 5. Continued

within rocks of the granite domain are transitional between those of the quartz monzonite and high-silica granite in that they are variably porphyritic, with euhedral poikilitic plagioclase (1–5 mm) and interstices that contain coarser quartz and orthoclase than in the quartz monzonite domain (Fig. 5d).

Whole-rock geochemistry

The lithological variation of the RBH plutonic complex is manifest in a wide compositional range from the RB gabbro (51 wt % SiO_2) to the high-silica granite (76 wt % SiO_2) of Huemul (Schaen *et al.*, 2017). Many major and trace elements (e.g. K_2O, Sr) vary monotonically with evolving SiO_2 content (Fig. 7). Yet some display distinct inflections; between 62 and 66 wt % SiO_2 marks the furthest extent in differentiation of RB compositions and the appearance of the least evolved Huemul rocks. At 66 wt % SiO_2 in variation diagrams of Ba, Zr, Hf and Eu, Huemul compositions bifurcate from the monotonic compositional variation of RB, with high-silica granite displaying strong depletions and quartz monzonite showing distinct enrichments in these elements along a tie-line of three tight clusters (Fig. 7). The granite is always halfway between the other two Huemul domains on variation diagrams. Huemul domains maintain this tie-line of tight clusters along all compositional arrays except for the rare earth elements (REE; excluding Eu). Apart from Eu, the Huemul high-silica granite domain evolves along highly scattered REE paths, decoupled from other trace elements (Fig. 7).

Mineral chemistry

In situ major, trace and rare earth element compositions were measured in minerals within eight hand samples, one from each domain of the RBH complex (Table 1) and two samples from the high-silica granite domain.

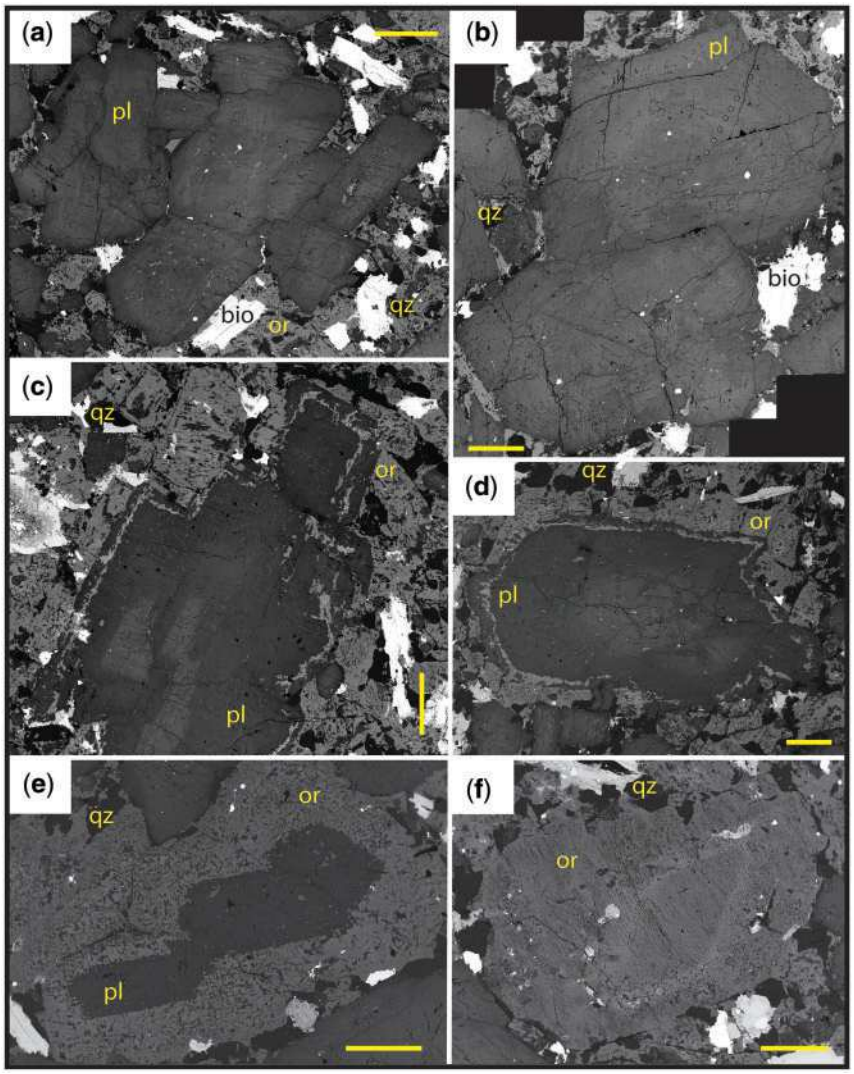

Fig. 6. Back-scattered electron (BSE) images of feldspar textures from the quartz monzonite domain of the Huemul pluton. (a, b) Synneusis clusters of zoned plagioclase. (c–e) Anti-rapakivi textures. (f) Euhedral orthoclase with bright BSE core. Scale bar represents 1 mm in all images.

Major elements were measured by electron probe microanalysis (EPMA) at the University of Wisconsin–Madison using either a CAMECA SX51 or SXFive field emission electron probe. This included analysis of 65 amphibole (348 spots), 133 plagioclase and orthoclase feldspar (1560 spots) and 32 biotite (200 spots) crystals. Major element compositions of minerals were obtained using a 1–5 μm diameter beam with an accelerating voltage of 15 keV. Trace elements were measured *in situ* by LA-ICP-MS at the University of California–Santa Barbara using an Agilent 7700S quadrupole ICP system following the methods of McKinney *et al.* (2015). LA spots (20 μm) were placed as close to or on top of EPMA spots whenever possible, calibrated using basaltic glass BHVO-2g as an external standard, and CaO or SiO_2 as an internal standard (obtained by EPMA). EPMA and LA-ICP-MS data were reduced respectively using the software 'probe for EPMA' (Donovan *et al.*, 2018) and IGOR Pro by WaveMetrics, Inc.

Amphibole

Amphibole from the RBH complex ranges from magnesiohornblende to pargasite, with local alteration to actinolite. Amphibole formulae based on 23 O atoms were calculated using the classification scheme of Hawthorne *et al.* (2012). Actinolite, inferred to be secondary, was filtered from the data and omitted from discussion or use in barometric calculations. Amphibole from the RB pluton has a range of Mg# (Mg/[Mg + Fe]) from 0·60 to 0·75, with each domain displaying distinct trends versus Si (Supplementary Data Table 1; supplementary data are available for downloading at http://www.petrology.oxfordjournals.org). In contrast, the majority of Huemul amphibole have lower Mg# from 0·46 to 0·59 and higher K contents. Mg# generally increases with Si content, whereas Al, K, and Ti decrease. Hornblende crystallization pressures of 0·9–2·2 ± 0·34 kbar were calculated for 91 analyses of RBH amphibole (with Fe# $<0{\cdot}65$ and $T < 800^{\circ}$C; Anderson &

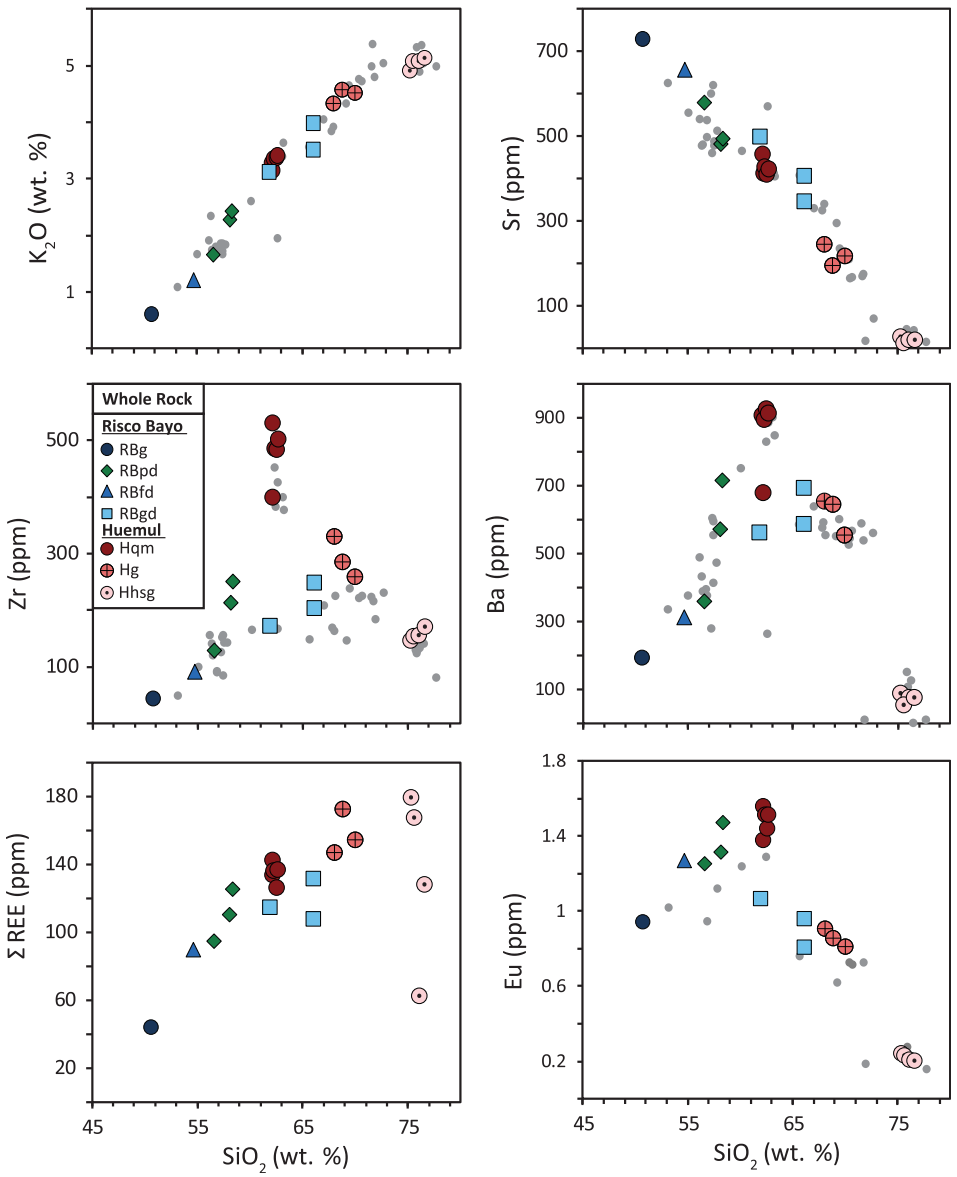

Fig. 7. Whole-rock major and trace element variation diagrams for rocks from the RBH plutonic complex. Small gray circles are RBH whole-rock data from Nelson *et al.* (1999). Domain abbreviations as in Table 1.

Smith, 1995) using the Al-in-Hbl barometric calibration of Mutch *et al.* (2016). This calibration is restricted to granitic rocks with amphibole + plagioclase + biotite + quartz + alkali feldspar + ilmenite/titanite + magnetite + apatite at the haplogranite solidus, conditions that are met by the quartz monzonite, granite, and granodiorite rocks. Amphibole from the granite and quartz monzonite domains varies over a wide compositional range, overlapping in Nb (~100 ppm) and Ce (~350 ppm) and generally increasing against Ti content (Fig. 8; Supplementary Data Table 2). Huemul amphiboles contain higher total REE abundances and lower Eu/Eu* than those from RB. Amphiboles from the granite and quartz monzonite display similar total REE abundances and Eu anomalies (Fig. 8). In contrast, the magnitude of the Eu anomaly varies by a factor of five in RB amphibole, with each hand sample forming its own field. Hand samples from each RB domain form distinct compositional arrays in their amphibole chemistry with contrasting and/or subparallel slopes in Nb, Zr, Ti, and REE (Fig. 8).

Biotite

Biotite from the three Huemul domains spans Mg# 0·40–0·62, generally inversely correlated to Al (~2·6–2·0 atoms per formula unit). TiO_2 and SiO_2 vary monotonically with Mg#; otherwise all biotites span the same range in K_2O (7–10 wt %) and NaO (0·04–0·35 wt %; Supplementary Data Table 3). Major element intracrystal zonation is absent, but the three Huemul domains preserve limited ranges in MnO such that quartz monzonite (0·05–0·30 wt %), granite (0·35–0·70 wt %) and

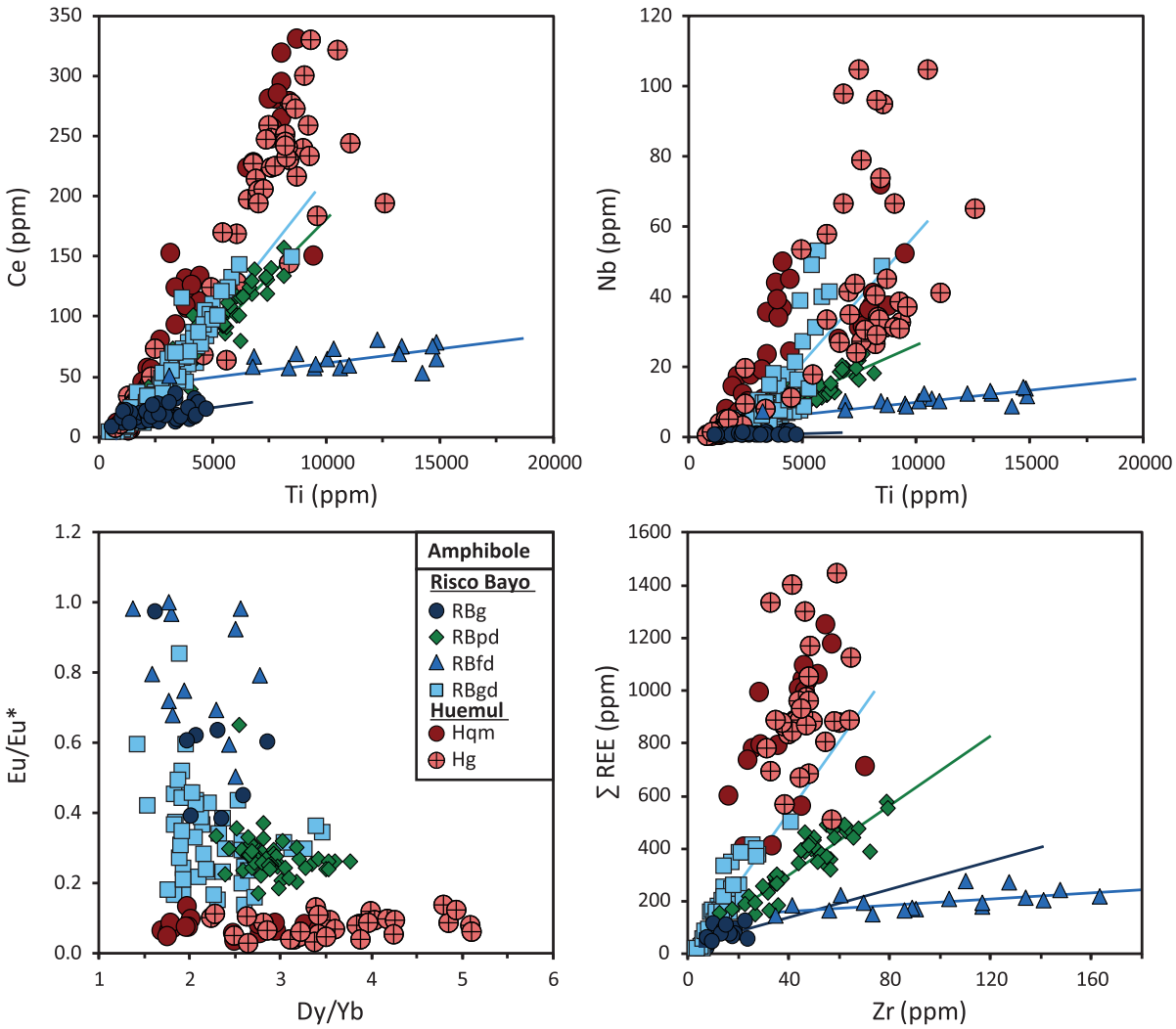

Fig. 8. Laser ablation trace element data for amphibole from the Risco Bayo–Huemul plutonic complex (Supplementary Data Table 2). Domains described in text. Crystals from one hand sample within each domain were analyzed. Trend lines through data arrays are colored by hand sample. $Eu/Eu^* = Eu_N/\sqrt{(Sm_N \times Gd_N)}$. Average 2σ uncertainties are smaller than symbol size. Domain abbreviations as in Table 1.

high-silica granite (0·20–0·30 wt %) form distinct fields versus Mg#. Biotite from the granite and quartz monzonite spans the same range in V (145–270 ppm), compared with the strong depletions in high-silica granite biotite (V = 7–18 ppm). A compositional gap in V separates the granite and quartz monzonite biotite from the high-silica granite (Fig. 9). The high-silica granite biotite is enriched in Rb, Nb, and Sc, but depleted in Cr, Co and Ba relative to the two other Huemul domains (Supplementary Data Table 4). Of all trace elements within Huemul biotite, Ba displays the widest range of compositions, from 7500 ppm in quartz monzonite to ≤100 ppm in the high-silica granite (Fig. 9).

Plagioclase

Coarse (3–5 mm) euhedral plagioclase from the quartz monzonite and granite is normally zoned, trending from $An_{50–56}$ interiors to more sodic rims ($An_{5–20}$; Supplementary Data Table 5). Anhedral fine-grained (≤1 mm) plagioclase in the matrix of both domains is more albite-rich ($An_{9–27}$), similar to the rim compositions of the larger euhedral crystals (Fig. 10). All plagioclase in the high-silica granite is albite ($An_{3–16}$). Risco Bayo plagioclase is more calcic with normally zoned euhedral crystals from the gabbro and granodiorite varying from $An_{85–89}$ interiors to ∼An_{30} rims. Plagioclase from the granodiorite and porphyritic diorite is slightly more evolved, with $An_{50–60}$ interiors zoning to $An_{15–20}$ rims. A small percentage of plagioclase within the granodiorite and porphyritic diorite contains bright BSE cores as calcic as $An_{75–85}$ (Fig. 10). Contrasting trace element variation is observed in plagioclase from the two plutons (Fig. 11; Supplementary Data Table 6). As a whole, plagioclase from RB proceeds from high to low Eu and Ba with decreasing An %, whereas Huemul plagioclase variation is positively correlated with these elements versus An content. RB plagioclases are generally more enriched in Sr compared with those in Huemul (≤1300 ppm; Fig. 11). Ba, Eu, and Sr all vary

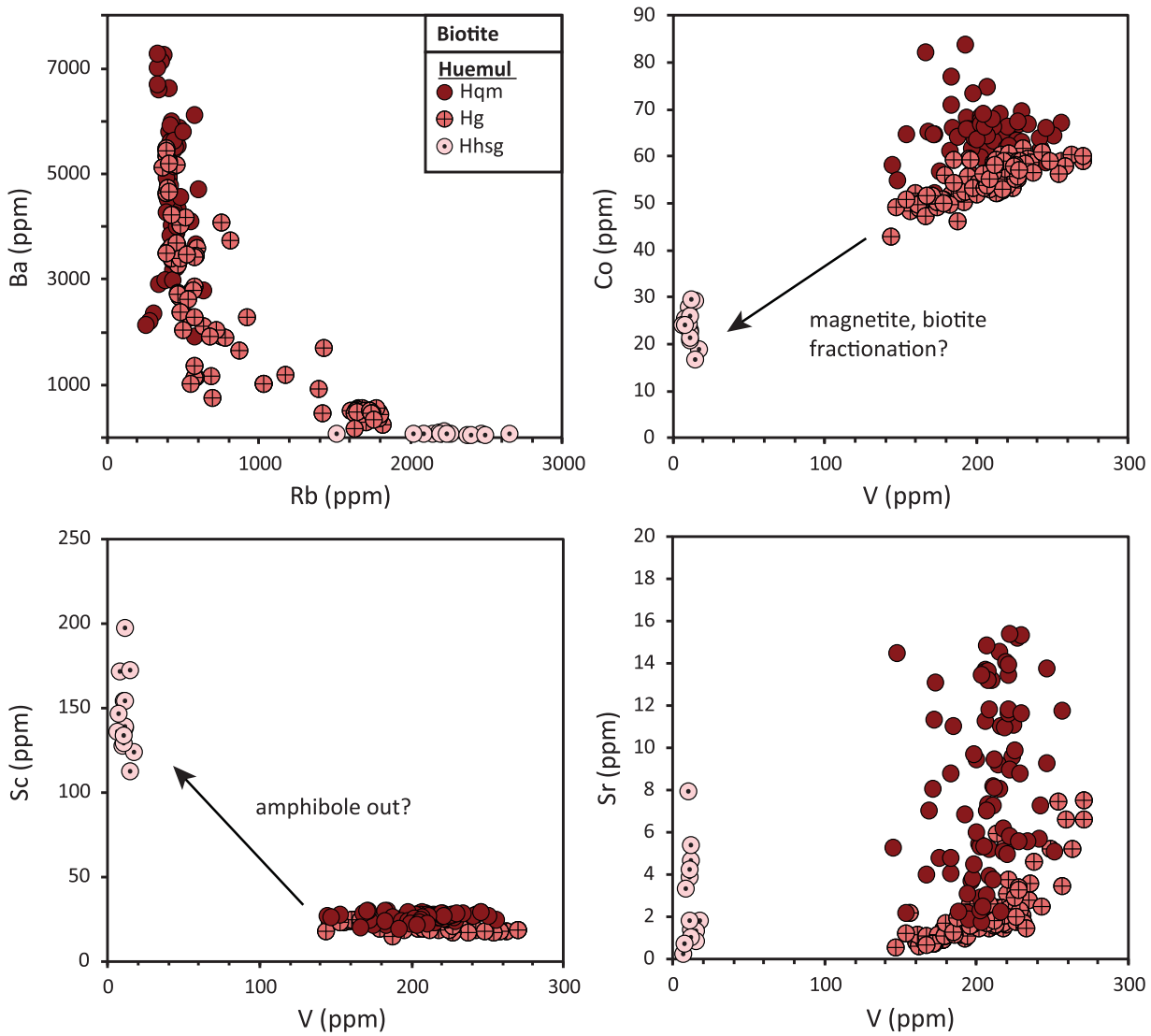

Fig. 9. Laser ablation trace element compositions of biotite from the Risco Bayo–Huemul plutonic complex (Supplementary Data Table 4). One hand sample from each domain was analyzed. Average 2σ uncertainties are smaller than symbol size. Domain abbreviations as in Table 1.

monotonically versus Ti in RB plagioclase, whereas hand samples from each domain display distinct trends and fields (Fig. 11). Plagioclase from the quartz monzonite and granite display similar ranges in Eu, Ba, and Sr concentrations, with the anhedral and interstitial populations in these domains approaching the highly depleted trace element compositions of the high-silica granite (Fig. 11).

Orthoclase

Alkali feldspar is present in all three Huemul domains, whereas in the Risco Bayo pluton it occurs only in the granodiorite. Euhedral alkali feldspar in the quartz monzonite has bright BSE cores ($Or_{48–89}$) that are generally zoned from low Or_{48} interiors to high $Or_{75–90}$ rims (Fig. 12). Euhedral orthoclase has the highest Ba (>6000 ppm) and Eu (>1·5 ppm) contents of all orthoclase, which display slight positive correlation with Ti and Sr (Fig. 13). Finer grained anhedral alkali feldspar in the matrix of the quartz monzonite domain is end-member orthoclase ($Or_{80–90}$; Fig. 12). Orthoclase in the granite is also anhedral and end-member ($Or_{80–90}$) in composition. Exsolved euhedral to subhedral alkali feldspar in the high-silica granite domain contains $Ab_{90–95}$ lamellae within unmixed $Or_{80–90}$. High-silica granite orthoclase is highly depleted in Sr, Ba, and Eu and displays the highest Rb (up to ~1000 ppm) among all other orthoclase (Fig. 13; Supplementary Data Table 7). Subhedral to anhedral orthoclase in the granodiorite is also end-member $Or_{80–90}$ and displays trace element trends with distinct fields in Sr, Eu, and Rb compared with Huemul (Fig. 13).

Whole-rock Sr isotopes

$^{87}Sr/^{86}Sr$ ratios were measured on 18 whole-rock powders from the RBH complex by thermal ionization mass

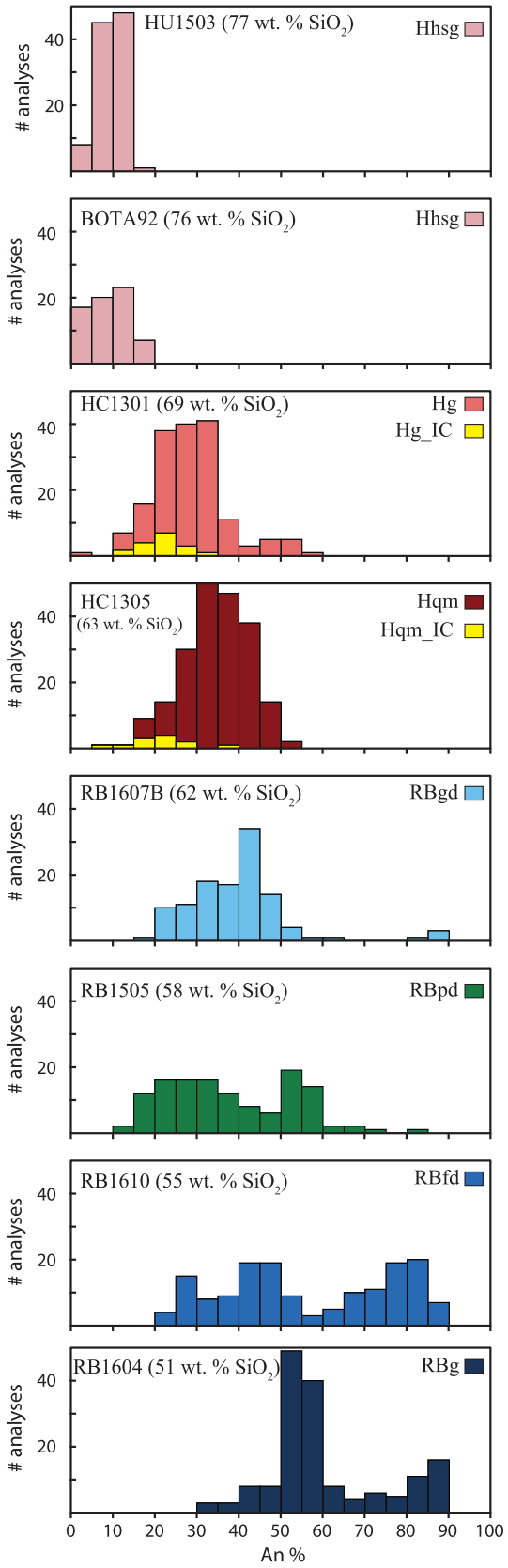

Fig. 10. Range of plagioclase compositions from the Risco Bayo–Huemul plutonic complex analysed by EPMA (Supplementary Data Table 5). Each panel represents data from one hand sample per domain (Table 1). IC, intercumulus feldspar. Domain abbreviations as in Table 1.

spectrometry (TIMS) at the University of Wisconsin–Madison (Table 2; Fig. 14) Samples were dissolved in a 5:1 solution of 29M HF + 14M HNO_3. Chemical separation of Rb and Sr followed the methods of Beard *et al.* (2013). Fifteen unspiked analyses were performed in 2015 and seven analyses were spiked using an enriched ^{87}Rb–^{84}Sr tracer in 2017 on samples with whole-rock Rb/Sr concentrations $\gg 1$. The $^{87}Sr/^{86}Sr$ ratios of unspiked samples have been corrected for post-crystallization decay of ^{87}Rb using their whole-rock Rb and Sr concentrations measured by ICP-MS, whereas the spiked samples were corrected using the isotope dilution concentrations. Mass spectrometry followed the method of Satkoski *et al.* (2017). The $^{87}Sr/^{86}Sr$ for standard NIST SRM-987 run concurrently with the unknowns had an average of 0·71028 ± 0·00001 (2SE; $n = 24$) over both analytical periods; Sr blanks averaged 23 pg. $^{87}Rb/^{85}Rb$ for standard NIST SRM-984 had an average of 2·594 ± 0·001 ($n = 5$) during 2017, accounting for a beta factor of 0·051845; Rb blanks averaged 51 pg. Whole-rock $^{87}Sr/^{86}Sr_i$ ranges from 0·70379 to 0·70413 for 17 samples when corrected to 6·2–7·0 Myr of *in situ* ^{87}Rb decay, based on $^{238}U/^{206}Pb$ zircon ages (Fig. 14; Schaen *et al.*, 2017). An aplitic dike sample (RB1518B) from the Huemul pluton resulted in a geologically unreasonable Sr isotopic ratio ($^{87}Sr/^{86}Sr_i < 0·701$) when age corrected using similar durations of *in situ* decay to other Huemul rocks. This suggests either diking occurred as late as 5·0 Ma or, more likely, post-emplacement mobilization of Rb or Sr affected this rock. Given the extreme elevation of Rb/Sr (435) in this dike we favor the latter scenario and do not discuss this sample further.

DISCUSSION

Schaen *et al.* (2017) used bulk-rock compositions and zircon petrochronology to argue that the rocks of the quartz monzonite domain are not representative of crystallized melt compositions, but rather the products of residual crystal concentration (silicic cumulates). Highly evolved rocks (76 wt % SiO_2) of the high-silica granite domain are hypothesized to be the solidified equivalents of rhyolitic melt that, as it was extracted from the mush, triggered passive concentration of crystals and formation of the quartz monzonite silicic cumulates (Schaen *et al.*, 2017). This model is based on complementary whole-rock enrichments (in quartz monzonite) and depletions (in high-silica granite) of Ba and Zr, along with mass balance of the Eu anomaly within these two domains at crystallinities (~50–70%) where melt extraction remains possible (e.g. Dufek & Bachmann, 2010). The narrow range of U–Pb zircon dates (spanning <300 kyr) and zircon trace element chemistry also support this unmixing model (Schaen *et al.*, 2017). The granite domain is hypothesized to be an intermediate composition possibly representative of the initial parental mush composition prior to unmixing. Here we use textures and mineral compositions to

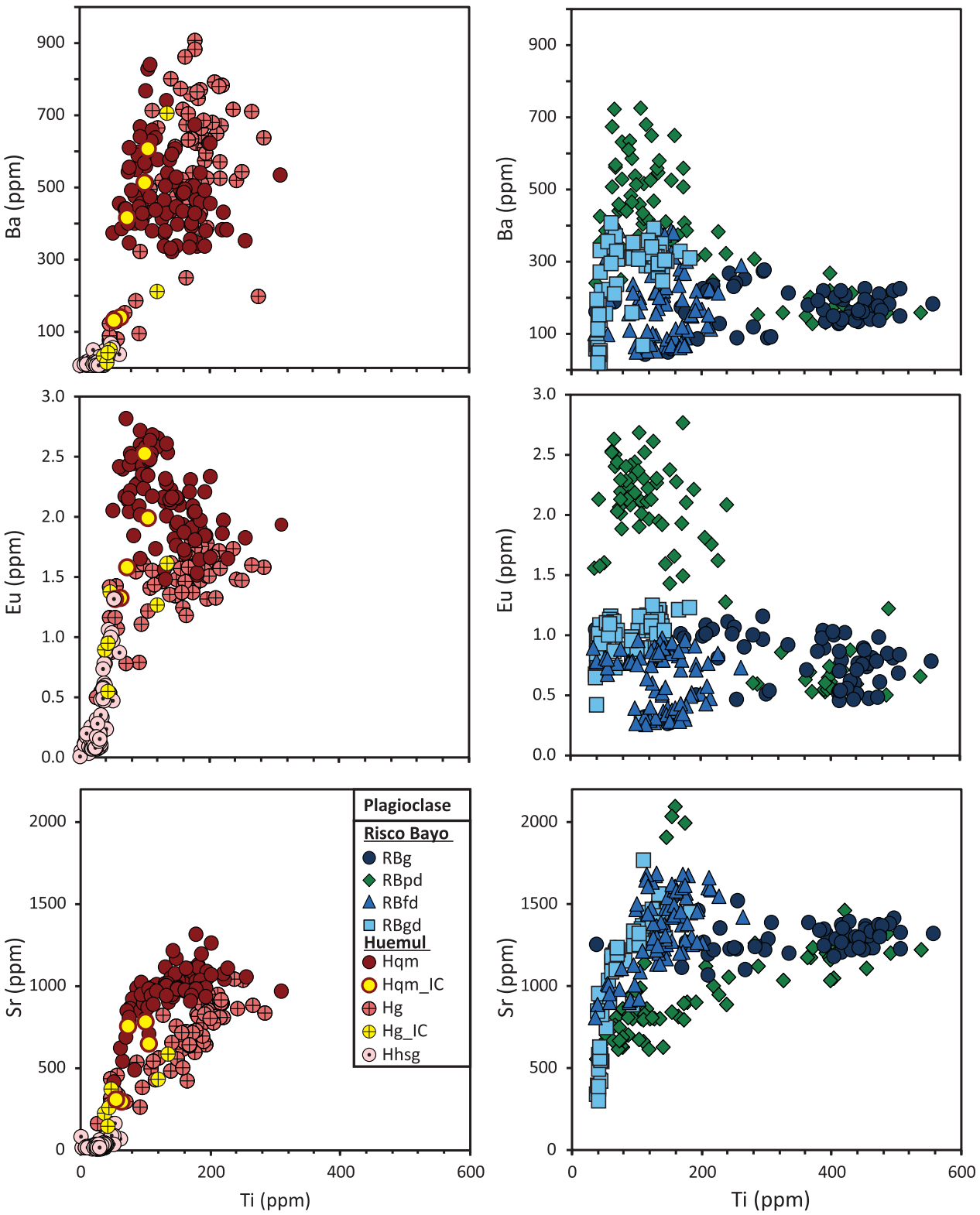

Fig. 11. Trace element concentrations in plagioclase from the Risco Bayo–Huemul plutonic complex (Supplementary Data Table 6). One hand sample from each domain was analyzed, apart from the Hhsg domain, which represents data from two hand samples 12 km apart. IC, intercumulus feldspar. Average 2σ uncertainties are smaller than symbol size. Domain abbreviations as in Table 1.

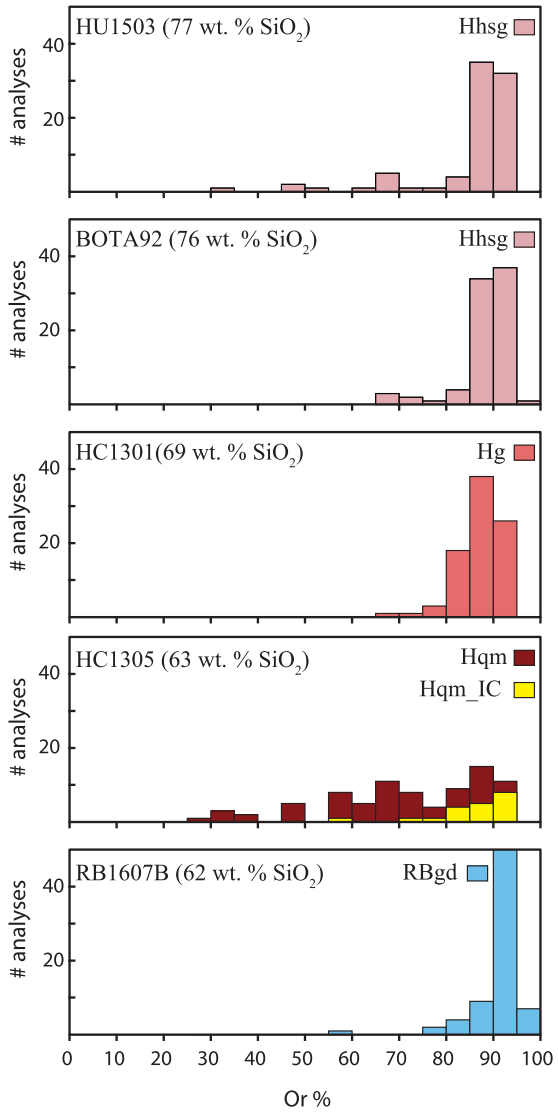

Fig. 12. Range of orthoclase compositions from the Risco Bayo–Huemul plutonic complex analysed by EPMA (Supplementary Data Table 5). Each panel represents data from one hand sample per domain. IC, intercumulus feldspar. Domain abbreviations as in Table 1.

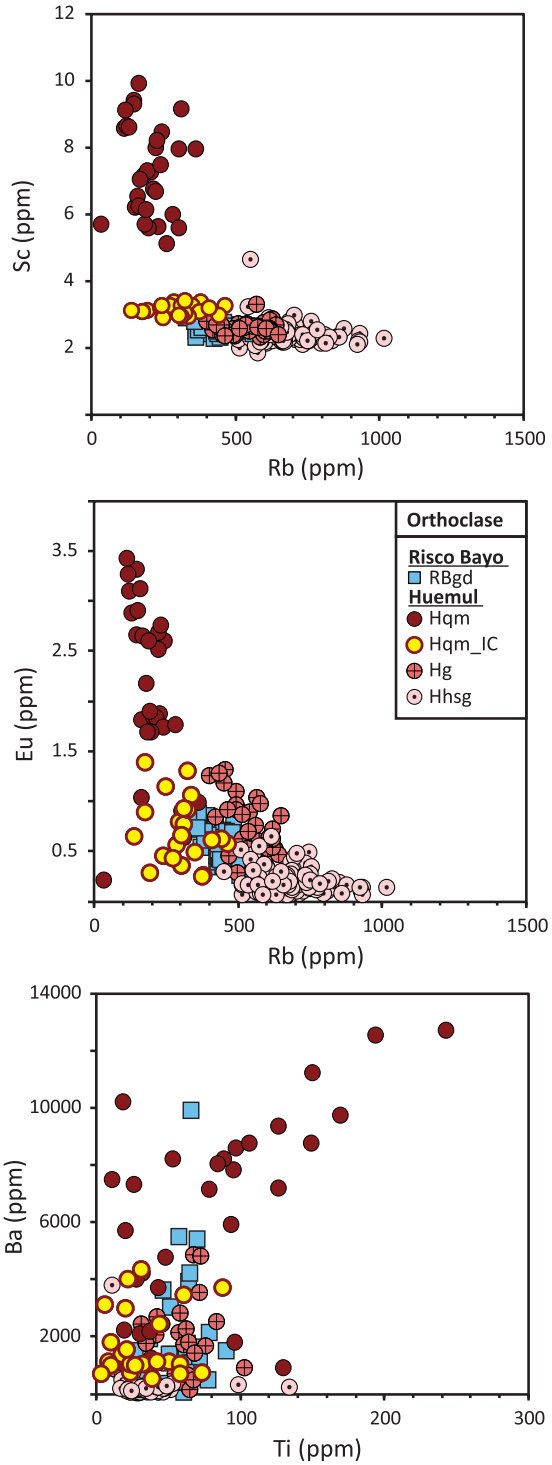

Fig. 13. Trace element concentrations in orthoclase from the Risco Bayo–Huemul plutonic complex (Supplementary Data Table 7). One hand sample from each domain was analyzed, apart from the Hhsg domain, which represents data from two hand samples 12 km apart. IC, intercumulus feldspar. Average 2σ uncertainties are smaller than symbol size. Domain abbreviations as in Table 1.

further explore this model. We then test whether silicic cumulate rocks of the quartz monzonite preserve remnants of trapped melt connected with the extraction of the high-silica granite.

Fingerprinting discrete magma injection

Some models for the formation and sustainability of silicic magma reservoirs within the upper crust involve injection of mafic magma (e.g. Hildreth, 1981, 2004; Hildreth & Wilson, 2007). Mafic magma flux may play a key role in priming the crust for subsequent differentiation of high-silica compositions (e.g. Hildreth, 2004) and reactivating magma reservoirs held in cold storage in a largely sub-solidus, crystalline state (e.g. Wark *et al.*, 2007; Cooper & Kent, 2014; Andersen *et al.*, 2017; Rubin *et al.*, 2017). Mafic enclaves within rhyolitic lavas are typically viewed as a clear indication that mafic and silicic magmas have interacted with one another (e.g. Bacon, 1986). We propose that the RB pluton represents the frozen remnants of discrete mafic injections ('mafic forerunners' of Hildreth, 2004) suggesting that a deeper

Table 2: Risco Bayo–Huemul whole rock Sr Isotopes

Sample	Pluton	Rb (ppm)	Sr (ppm)	Rb/Sr	$^{87}Sr/^{86}Sr_{measured}$	%SE	$^{87}Sr/^{86}Sr_i$	$^{87}Rb/^{86}Sr$
Unspiked analyses								
RB-15-02A	RB	113·77	481·41	0·24	0·70418	0·0007	0·70412	0·68
RB-15-09	RB	173·75	345·81	0·50	0·70421	0·0007	0·70406	1·45
RB-15-03B	RB	53·93	577·26	0·09	0·70406	0·0007	0·70404	0·27
RB-15-05	RB	87·37	491·54	0·18	0·70417	0·0008	0·70412	0·51
RB-15-05	RB	87·37	491·54	0·18	0·70417	0·0007	0·70413	0·51
RB-15-06	RB	153·37	405·39	0·38	0·70415	0·0008	0·70404	1·09
HC-13-05	H	120·00	409·00	0·29	0·70418	0·0007	0·70411	0·85
HC-13-01	H	239·00	193·00	1·24	0·70439	0·0007	0·70408	3·58
HU-15-01A	H	182·67	243·18	0·75	0·70427	0·0007	0·70408	2·17
RB-15-01	H	131·03	411·06	0·32	0·70420	0·0007	0·70412	0·92
RB-15-07	H	135·23	419·58	0·32	0·70419	0·0006	0·70411	0·93
RB-15-11	H	131·24	425·22	0·31	0·70420	0·0009	0·70412	0·89
RB-15-11	H	131·24	425·22	0·31	0·70419	0·0007	0·70411	0·89
RB-15-13	H	228·64	215·90	1·06	0·70438	0·0008	0·70412	3·06
RB-15-03A	H	112·17	455·68	0·25	0·70419	0·0008	0·70412	0·71
ID-spiked analyses								
RB-15-15	H	284·88	25·16	11·32	0·70687	0·0007	0·70399	32·75
HU-15-03	H	252·12	17·42	14·48	0·70768	0·0010	0·70400	41·88
BOTA92	H	270·66	15·91	17·01	0·70822	0·0007	0·70389	49·21
HU-15-04	H	266·59	9·98	26·70	0·71064	0·0007	0·70384	77·27
HU-15-04	H	263·04	9·83	26·75	0·71064	0·0006	0·70382	77·42
RB-15-18B	H	412·12	1·00	412·58	0·78939	0·0015	0·70396	1203·17

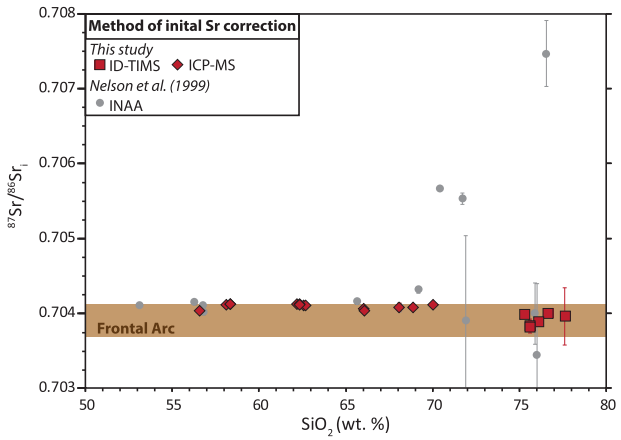

Fig. 14. Whole-rock $^{87}Sr/^{86}Sr_i$ vs wt % SiO_2 for the Risco Bayo–Huemul plutonic complex (Table 2). Red symbols are from this study; gray circles are from Nelson *et al.* (1999). Brown field shows range of $^{87}Sr/^{86}Sr_i$ of lavas from the adjacent frontal arc volcano Tatara–San Pedro (Davidson *et al.*, 1987, 1988). The 2σ error bars represent uncertainty in the Rb/Sr ratio propagated during age correction.

source region was actively producing partial melts for ~700 kyr prior to the formation and unmixing of the Huemul parental magma (Schaen *et al.*, 2017). This scenario is supported by field observations of sharp magmatic contacts in RB (Fig. 3), implying injection of discrete pulses of magma (Fig. 2). Additional support for this hypothesis is observed in RB amphibole trace element chemistry, where there are notable contrasts in Ti, Nb, Ce, and ∑REE (Fig. 8) such that subparallel arrays reflect discrete intrusions of successive magma batches as has been suggested for other plutons by Barnes *et al.* (2016*b*). If the amphibole chemistry is taken as a proxy for melt evolution, then RB magmas evolved along different fractionation trends, indicative of episodic mafic injection prior to mush formation. Moreover, amphibole crystallization probably occurs post-emplacement as indicated by the shallow barometry. Additionally, RB amphibole encompasses several discrete fields in Eu/Eu* vs Dy/Yb space (Fig. 8), very similar to fields seen in the same trace element ratios within zircon from the same RB hand samples (Schaen *et al.*, 2017). A similar trend is also evident in RB plagioclase (Fig. 11), wherein hand sample data form contrasting arrays, albeit with more scatter than for the amphibole. Abundant mafic enclaves within RB and Huemul suggest mingling and interaction of mafic and silicic magmas. However, the distinct fields and unique variation in mineral compositions defined by each hand sample (Figs 8 and 11) imply that successively intruded RB magmas evolved separately. We take these relationships in RB to signify that pulses of mafic to intermediate magma were emplaced adjacent to one another, episodically, prior to crystal–liquid segregation processes in the younger Huemul pluton.

Compositional evidence of melt extraction

Huemul whole-rock unmixing trends (Schaen *et al.*, 2017) are denoted by linear arrays defined by the three domains, with trace element enrichments in quartz monzonite complemented by depletions in the high-silica granite (Fig. 7). These whole-rock unmixing trends are mimicked in their mineral chemistries, providing additional evidence of unmixing. For example, quartz monzonite plagioclase is enriched in compatible elements (e.g. Ba, Sr, Eu) relative to depletions in high-silica granite plagioclase (Fig. 11). A similar relationship is seen in Huemul orthoclase in Ba, Eu, and Sc (Fig. 13). Huemul biotite displays similar variation with a

compositional gap in V mimicking the gap in whole-rock compositions between the granite and high-silica granite domains (Figs 7 and 9). In volcanic rocks, compositional gaps at these silica concentrations have been interpreted to reflect rhyolite melt extraction from intermediate residues (Brophy, 1991; Dufek & Bachmann, 2010). The presence of such a gap in Huemul biotite compositions may also record melt extraction (Fig. 9). Enrichments of Sc in high-silica granite biotite suggest that amphibole (Kd_{Sc} amph = 14; Bacon & Druitt, 1988) was removed from the liquidus at shallow depths, concurrent with the hypothesized melt extraction (Fig. 9), probably at the expense of biotite stabilization. The tight range in feldspar compositions from two samples of the high-silica granite separated by 14 km (Figs 11 and 13) along with identical bulk-rock compositions and zircon petrochronology (Schaen *et al.*, 2017), signifies that the high-silica granite domain is at least 14 km long and interconnected at depth (Fig. 2). The extreme depletions in Ba, Eu, and Sr within high-silica granite minerals support their crystallization from a large volume (~70 km^3 or more) of highly fractionated melt resembling rhyolite (e.g. Hildreth, 2004).

The $^{87}Sr/^{86}Sr_i$ ratios (0·70379–7·0413) in RBH rocks, including those where the $^{87}Rb/^{86}Sr$ was determined by isotope dilution (ID)-TIMS, fall within the narrow range of the active frontal arc volcano Tatara–San Pedro and other volcanic centers within this sector of the Andes (Fig. 14; Andersen *et al.*, 2017). The narrow range of $^{87}Sr/^{86}Sr_i$ within RBH rocks is consistent with the unmixing hypothesis, rather than an origin via assimilation or mixing within highly radiogenic Paleozoic to Mesozoic lower crust (Lucassen *et al.*, 2004), as suggested by Nelson *et al.* (1999).

Tracking mineral populations of crystal accumulation

Chemically and temporally identical zircon (within the uncertainty of laser ablation U–Pb geochronology of ~4%) from the three Huemul domains was taken as evidence of crystal accumulation in rocks with contrasting bulk-rock compositions (Schaen *et al.*, 2017). It is suggested that this zircon population crystallized from an initially granitic parent magma prior to the unmixing and subsequent crystallization of more evolved zircon. Here we observe an analogous relationship in amphibole, feldspar, and biotite within domains of the Huemul pluton. Amphibole from the quartz monzonite and granite spans similar ranges in Nb, Ti, Zr, and REE within overlapping fields (Fig. 8). Additionally, many biotite analyses from the quartz monzonite and granite are compositionally similar in Ba, Rb, V, and Sc content (Fig. 9). This is also true in quartz monzonite and granite plagioclase, which overlap in Ba and Eu contents (Fig. 11). These findings imply, as in zircon, that a chemically similar mineral population was present in the granite and quartz monzonite magma prior to when stark contrasts in whole-rock compositions were generated. We suggest that the similar mineral populations in the granite and quartz monzonite crystallized from the same parental magma prior to melt extraction and concurrent unmixing. Their presence in domains with contrasting bulk major and trace element compositions is additional support of crystal accumulation within the quartz monzonite.

Huemul rocks also comprise chemically distinct mineral populations of textural significance. For example, euhedral orthoclase within the quartz monzonite contains bright BSE cores (Figs 5a and 6) that are enriched in Ba, Eu, and Sc compared with the anhedral interstitial matrix orthoclase population from the same rock (Fig. 13). Accumulation of this early formed population of orthoclase may in part be responsible for this domain's enriched Ba whole-rock signatures (Fig. 7; Schaen *et al.*, 2017). Compositions of plagioclase and orthoclase from the anhedral interstitial matrix populations within the quartz monzonite and granite approach the Ba, Ti, Eu, and Sc contents of coarse-grained euhedral orthoclase from the high-silica granite. If high-silica granite rocks formed via melt extraction, preservation of feldspar compositions with similar trace element contents in the interstices of the quartz monzonite and granite rocks suggests that the interstitial matrix within these domains shares a common origin with this extracted melt.

Textural indicators of crystal accumulation

It is well accepted that crystal accumulation in mafic and ultramafic plutons can result in widespread compositional and textural layering (e.g. Wager *et al.*, 1960; Wager, 1963; Wager & Brown, 1968; O'Driscoll & VanTongeren, 2017, and references therein). Wager *et al.* (1960) defined the term 'cumulate' as related to a specific process, gravitational crystal settling, in the formation of rocks with foreign accumulated crystals (cumulus minerals) cemented together by a finer-grained interstitial assemblage inferred to represent trapped liquid (intercumulus minerals). Irvine (1982) redefined this terminology so that 'A cumulate is defined as an igneous rock characterized by a framework of touching mineral crystals and grains that evidently were concentrated through fractional crystallization of their parental magmatic liquids', importantly unrestrictive of the physical process by which crystals accumulated. This definition accounts for known discrepancies associated with gravitational settling in mafic cumulates (e.g. cumulus plagioclase should float, not sink in dense mafic liquids) and is amenable for use within granitic systems (i.e. silicic cumulates) whereby crystal accumulation–melt segregation probably occurs via a combination of different processes (see Holness, 2018, for a recent review) such as (1) volatile-induced filter pressing (e.g. Anderson *et al.*, 1984; Sisson & Bacon, 1999; Boudreau, 2016; Parmigiani *et al.*, 2016), (2) magma recharge (e.g. Bachmann *et al.*, 2007; Charlier *et al.*, 2007; Bergantz *et al.*, 2015), and (3) segregation driven by external

tectonic stress (e.g. Sawyer, 2000; Rosenberg, 2001; Garibaldi *et al.*, 2018).

Following the definition of Irvine (1982), we suggest that the porphyritic textures preserved in rocks of the quartz monzonite are cumulate in origin (Fig. 5a and c). This is based upon the following observations in quartz monzonite rocks.

(1) These rocks comprise a framework of touching euhedral minerals dominated by plagioclase along with biotite, orthoclase, and hornblende (Fig. 5a and c). It is this touching framework that suggests that the network of earlier-formed euhedral minerals are cumulus (Irvine, 1982; Miller & Miller, 2002; Wiebe *et al.*, 2002; Harper *et al.*, 2004; Collins *et al.*, 2006).

(2) The fine-grained interstitial assemblage is reminiscent of frozen pore fluid (Morse, 1982; Sparks *et al.*, 1985) similar in appearance to micro- and mesoscopic textures thought to represent trapped melt in granitic systems (Wiebe & Collins, 1998; Wiebe *et al.*, 2002; Vernon & Paterson, 2008; Vernon & Collins, 2011). This interstitial assemblage is composed of an anhedral and unzoned haplogranite mineralogy (quartz, Ab-rich plagioclase and orthoclase) resembling quenched felsic melt.

(3) Synneusis ('swimming together') of quartz and plagioclase is interpreted to result from crystal accumulation (Vance, 1969; Beane & Wiebe, 2012; Graeter *et al.*, 2015). Here we suggest the synneusis of zoned euhedral cumulus plagioclase (Fig. 6a and b) reflects the concentration of crystals owing to segregation of interstitial melt.

(4) Anti-rapakivi textures in feldspars (Fig. 6c–e) have been interpreted as the product of isobaric *in situ* fractional crystallization (Tuttle & Bowen, 1958; Stewart & Roseboom, 1962; Abbott, 1978). The presence of some quartz monzonite cumulus feldspars with anti-rapakivi textures supports a role for crystal–liquid fractionation concurrent with melt extraction.

(5) Imbrication of undeformed cumulus plagioclase (Fig. 5c) is consistent with concurrent crystal accumulation and interstitial melt removal (Shelley, 1985; Philpotts & Asher, 1994; Vernon, 2000). This imbrication of plagioclase is similar to observations of accumulated, compressed K-feldspar megacrysts, which, in some cases, have been interpreted to result from compaction (Paterson *et al.*, 2005; Vernon & Paterson, 2008; Vernon & Collins, 2011).

Importantly, all rocks from the quartz monzonite that display the above textural characteristics of crystal accumulation also have cumulate bulk-rock geochemical signatures (Schaen *et al.*, 2017).

Intercumulus matrix composition

The composition and proportion of trapped melt within plutonic rocks has previously been estimated via major and trace element modelling of whole-rock compositions (e.g. Bédard, 1994; Leuthold *et al.*, 2014; Lee & Morton, 2015; Barnes *et al.*, 2016*a*), quantification of textural relationships using various imaging techniques [e.g. EDS, BSE, cathodoluminescence (CL); e.g. Wiebe *et al.*, 2007; Graeter *et al.*, 2015; Fiedrich *et al.*, 2017], along with terminal porosity constraints within stratified mafic intrusions (e.g. Morse, 1979). Here we are interested in texturally significant portions of the quartz monzonite silicic cumulate rocks. We leverage our phase maps and mineral compositional data from a porphyritic hand sample of the quartz monzonite to perform a high spatial resolution calculation with the goal of estimating the composition of the interstitial matrix from this domain (Fig. 5b). The interstitial matrix (anhedral orthoclase, quartz, and plagioclase) of quartz monzonite hand sample HC1305 forms 41·6 ± 8 area % of the thin section, whereas the euhedral 'cumulus' network (euhedral plagioclase, biotite, orthoclase, and amphibole) is 58·4 ± 12 area % (Fig. 5b). This distinction is determined on a textural basis such that all fine-grained (≤1 mm) and anhedral minerals within the interstitial matrix are considered 'intercumulus' and coarse (2–5 mm) euhedral minerals are considered 'cumulus' (Supplementary Data Table 8). We have added conservative 20% uncertainties on these estimates to account for the Ab-rich rims of euhedral cumulus plagioclase crystals, which may be considered intercumulus (e.g. Graeter *et al.*, 2015).

For our calculations, we assume that area fraction is equal to volume fraction, then use mineral densities to convert to mass fraction for each phase in HC1305 (Fig. 5b; Supplementary Data Table 8). Using EPMA data, we assign representative major element oxide (SiO_2, Al_2O_3, etc.) compositions to each phase within HC1305, separating cumulus minerals from those in the matrix. The quantitative mass fractions from EDS phase maps (Fig. 5) are then used to estimate a bulk composition of the intercumulus matrix via sum product calculation (Supplementary Data Table 8). As proof of concept, we first use the above approach to calculate whole-rock compositions for a hand sample from each Huemul domain with an EDS phase map (Fig. 5). CIPW normative mineral assemblages were calculated using these modelled bulk-rock compositions and normalized Qz–Ab–Or assemblages and are plotted on the water-saturated haplogranite ternary (Fig. 15). Abundant miarolitic cavities in the high-silica granite (Fig. 3a) imply the presence of a volatile phase, justifying the use of the water-saturated system. That the modelled bulk compositions from EPMA results are consistent with whole-rock XRF analyses indicates that estimating bulk compositions using mineral data is a practical approach (Fig. 15). Rocks of the high-silica granite plot at the water-saturated granite minimum between 1 and 2 kbar, pressures consistent with Al-in-Hbl barometry of the other Huemul domains that imply solidification at about 3·7–7·2 km depth. Notably, rocks of the quartz monzonite and granite domains do not plot near cotectic minima, and hence are non-liquid bulk compositions that form a mixing line with high-silica granite. These observations, coupled with whole-rock compositions, are

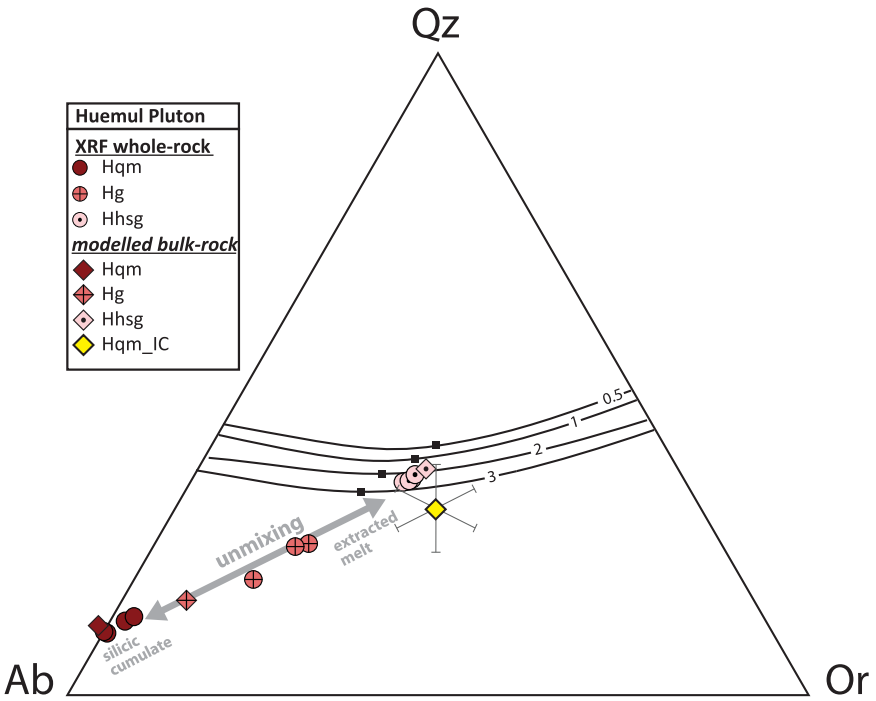

Fig. 15. Qz–Ab–Or H_2O-saturated haplogranitic ternary. Lines are cotectics and black squares are locations of minimum melts at a given pressure (kbar). Modified from Blundy & Cashman (2001) using the data of Tuttle & Bowen (1958), Luth *et al.* (1964) and Ebadi & Johannes (1991). Circles are XRF whole-rock analyses from the Huemul pluton that have been converted to CIPW normative assemblages, normalized to Qz–Ab–Or and corrected for anorthite influence, following Blundy & Cashman (2001). Diamonds are modelled bulk compositions using modal abundances from phase maps (Fig. 5) and EPMA chemistry (see text). Hqm_IC represents the intercumulus matrix of sample HC1305 from the Hqm (Fig. 16) with 10% uncertainties. Domain abbreviations as in Table 1.

consistent with unmixing of a single parental magma (Fig. 7; Schaen *et al.*, 2017).

Deviation from these tightly clustered linear unmixing trends in Huemul domains is evident in REE whole-rock variation diagrams (Fig. 7). That the REE are decoupled from other trace elements (Fig. 7), with high-silica granite samples forming a scattered field, suggests that melt extraction occurred at the granite minimum, where small variations in temperature can result in large changes in crystallinity (Tuttle & Bowen, 1958). The variable REE compositions of the high-silica granite rocks most probably result from slight differences in the modal proportions of zircon and apatite crystallization concurrent with melt extraction.

Separating the euhedral cumulus framework in the quartz monzonite, we performed the above major element calculation for just the interstitial matrix of HC1305 (Fig. 15). The modelled bulk composition of the quartz monzonite intercumulus matrix has a SiO_2 content of 75 wt % and plots on top of the high-silica granite cluster at the granite minimum, within a conservative 10% uncertainty in this estimate. Thus, the matrix preserved in the porphyritic quartz monzonite sample HC1305 is representative of a high-silica granite melt similar in major element composition to the rocks of the high-silica granite, which cooled to the granite minimum.

To estimate the bulk trace-element content of the quartz monzonite intercumulus matrix we rely on the compositions of anhedral interstitial feldspars. Plagioclase compositions can be used to calculate the equilibrium melt from which they crystallized via temperature–An-dependent partitioning of trace elements (Blundy & Wood, 1991; Bindeman *et al.*, 1998). We use the thermodynamic model rhyolite-MELTS (Gualda *et al.*, 2012) to produce An versus temperature curves for the RBH system and then determine partition coefficients for Ba and Sr following the calibration of Bindeman *et al.* (1998). We use these An-dependent partition coefficients to calculate the Ba and Sr content of equilibrium melts from our measured LA-ICP-MS plagioclase compositions (Fig. 11). Equilibrium melt compositions determined from the majority of intercumulus plagioclase from quartz monzonite (HC1305) and granite (HC1301) have $\leq$75 ppm Ba and $<$50 ppm Sr, which overlap with the whole-rock content of the high-silica granite hand samples (Fig. 7) and those calculated using high-silica granite plagioclase (BOTA92; Fig. 16a).

Without the coupled solid solution that makes plagioclase partitioning a function of An content (Blundy & Wood, 1991), calculating the trace element content of the equilibrium liquid (C_L) using orthoclase compositions (C_S) is more straightforward and can be estimated with a simple distribution coefficient (K_D) relationship ($C_L = C_S/K_D$). Melt compositions determined from orthoclase within the quartz monzonite intercumulus matrix have average Ba and Sr contents of 102 ppm and 25 ppm, respectively (Fig. 16b). Like the estimates

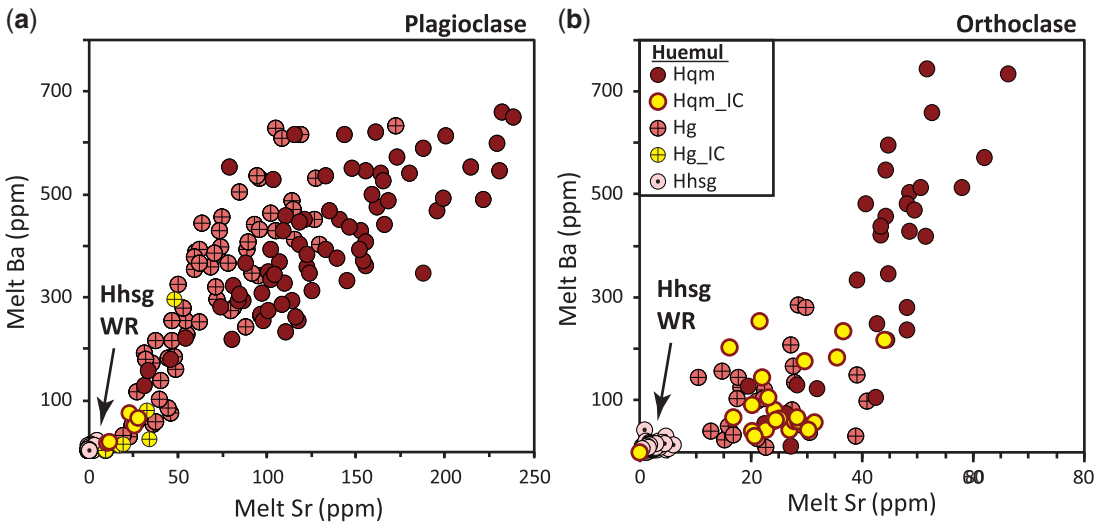

Fig. 16. Equilibrium melt compositions calculated via (a) An-dependent plagioclase compositions following Bindeman *et al.* (1998) and (b) orthoclase compositions using a $Kd_{Ba} = 17{\cdot}1$ and $Kd_{Sr} = 7{\cdot}4$ (Bachmann *et al.*, 2005). Domain abbreviations as in Table 1.

using plagioclase, the melt determined from orthoclase compositions within the quartz monzonite intercumulus matrix overlaps in Ba content with estimates made from high-silica granite orthoclase (<100 ppm Ba; Fig. 16b) and high-silica granite whole-rock compositions (Fig. 7). The Sr content determined from quartz monzonite orthoclase (<50 ppm) also approaches high-silica granite estimates (<10 ppm Sr) and whole-rock compositions (<26 ppm Sr). Slight discrepancies between the Sr melt composition estimated using plagioclase and orthoclase (Fig. 16) probably reflect minor variations in the choice of partition coefficients when using two different techniques for these calculations. Nevertheless, the melt compositions estimated from fine-grained, anhedral, interstitial feldspar within the porphyritic quartz monzonite and semi-porphyritic granite (Fig. 5d) suggest that both domains contain matrix material that crystallized from a high-silica granite melt highly depleted in Ba and Sr. We interpret the major and trace element estimates for the quartz monzonite intercumulus matrix (75 wt % SiO_2 and depleted Ba and Sr) to be a record of trapped melt that was extracted upon formation of the high-silica granite domain over the 100–300 kyr crystallization duration of this domain (Schaen *et al.*, 2017). Euhedral quartz monzonite orthoclase and plagioclase that preserve 550–700 ppm Ba melt compositions (Fig. 16) imply that these feldspars crystallized from a parental magma comparable in bulk composition with the granite, whose whole-rock Ba content is identical (Fig. 7). The granite domain was used as a starting composition in a bulk-rock melt-extraction model (Schaen *et al.*, 2017) and is our best estimate of a Huemul parental magma from which all three domains formed via unmixing. That this starting composition is preserved in the quartz monzonite feldspars with the appropriate euhedral textures is taken as strong support of crystal accumulation of the predicted parental mineral population.

Locally abundant miarolitic cavities within the high-silica granite (Fig. 3a) reflect saturation of melt with a magmatic vapor phase at low pressure. We envision an essential role for H_2O in the evolution of the high-silica granite domain in two ways. First, H_2O dissolved in the high-silica intercumulus melt dramatically lowers its viscosity, thereby enhancing its ability to flow through the crystalline mush framework. Second, numerical simulations of multi-phase fluid dynamics reveal that the buoyant flux of an exsolved magmatic vapor phase, and probably some of the coexisting melt, through the confined pore space in a rigid crystal-rich mush is greatly enhanced (Parmigiani *et al.*, 2016). Moreover, the magmatic vapor phase will accumulate in bubbles that concentrate in the overlying crystal-poor melt, thereby increasing magma viscosity and enhancing cooling and solidification (Parmigiani *et al.*, 2016; Edmonds & Wallace, 2017).

CONCLUSIONS

The RBH complex records textural and mineral compositional evidence that supports previous findings of upper crustal differentiation within a plutonic system, from precursory flux of mafic to intermediate magma pulses to near end-members of rhyolite melt extraction (Fig. 17). All rocks from the quartz monzonite domain that display non-liquid geochemical signatures also have porphyritic textures defined by a euhedral cumulus framework and evolved interstitial matrix of haplogranite mineralogy. We propose that this relationship, along with other textural features of crystal accumulation including synneusis, imbrication of euhedral plagioclase, and anti-rapakivi textures, further implies that the quartz monzonite rocks are inherently cumulate and have lost interstitial liquid. That these rocks contain 62 wt % SiO_2 makes them silicic cumulates and requires their formation via extraction of high-silica melt comparable in major and trace element chemistry with the

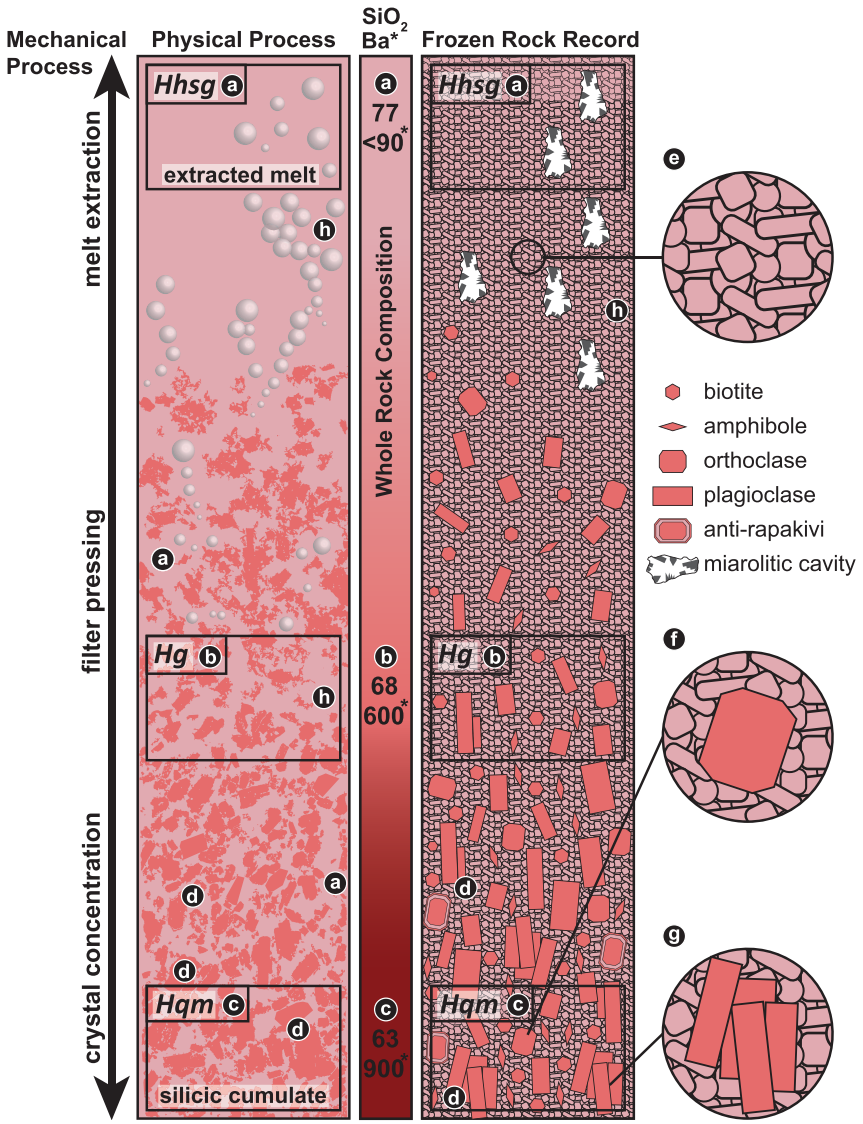

Fig. 17. Conceptual petrogenetic model (not to scale) of Huemul pluton formation via filter pressing, driven by volatile exsolution and horizontal crustal shortening (Garibaldi *et al.*, 2018). Crystal orientation is consistent with the fabric work of Garibaldi *et al.* (2018) showing feldspar alignment parallel to melt transport direction, in this case, upwards. Colors in all panels reflect bulk composition. (a–c) Melt extraction–cumulate formation manifest in complementary whole-rock compositions (SiO_2 in wt %, Ba in ppm; Fig. 7) and crystal–liquid textural relationships (Fig. 5) between the three domains of the Huemul pluton; (d) textural evidence for crystal concentration and melt extraction, including a touching framework of euhedral minerals, clustering of earlier-formed plagioclase crystals, and anti-rapakivi feldspars (Fig. 6); (e) finer-grained anhedral to subhedral haplogranite depleted in Ba (Fig. 16); (f) euhedral orthoclase (6000–12 000 ppm Ba; Fig. 13) crystallized from ~600 ppm Ba parent magma (Fig. 16); (g) clustering of euhedral plagioclase (Fig. 6) crystallized from ~600 ppm Ba parent magma (Fig. 16); (h) volatile saturation aids melt extraction by gas fracturing in crystal-rich layers and buoyant bubble rise in crystal-poor regions; when cooled these bubbles form dense zones of miarolitic cavities (Fig. 3a). Domain abbreviations as in Table 1.

high-silica granite domain. Remnants of this extracted high-silica granite melt are preserved as 75 wt % SiO_2 intercumulus matrix within these porphyritic rocks (Fig. 17). Model calculations suggest that the intercumulus matrix of quartz monzonite rocks records Ba- and Sr-depleted rhyolitic melt that reached the granite minimum at epizonal depths, comparable in composition and mineralogy with the high-silica granite domain. Importantly, the euhedral cumulus framework of quartz monzonite rocks also records the predicted Huemul parent magma prior to unmixing.

The common geochemical signatures of feldspar in high-silica granite samples located 14 km apart are bolstered by zircon petrochronology and imply that this domain formed a large ~70 km^3 (if scale-invariant and 1·2 km thick; McCaffrey & Petford, 1997) body of water-saturated, high-silica granite melt in the roof zone of the complex at depths of <7 km. Depleted Ba, Eu, and Sr within plagioclase, orthoclase, and biotite support this domain's role as fractionated and extracted rhyolitic melt. Projections into the haplogranite ternary imply that rocks of the high-silica granite are minimum melts.

The mineral compositional data from the three Huemul domains mimics their whole-rock trends of unmixing from a common granitic parent. The restricted range of whole-rock $^{87}Sr/^{86}Sr_i$ data reinforces that this upper crustal magma reservoir had minimal interaction with highly radiogenic crust and supports the unmixing hypothesis.

Distinct compositional arrays of amphibole from older RB domains suggest that these magmas did not interact chemically but rather represent discrete pulses. The amphibole chemistry and sharp magmatic contacts imply a role for RB-type magma flux in the form of incremental emplaced mafic to intermediate magma batches prior to the initiation of crystal–liquid separation processes in Huemul (Fig. 17). Abundant mafic enclaves within the quartz monzonite and granite reflect this type of interaction. The RBH plutonic complex embodies evidence in the form of compositional variation of whole-rocks and minerals, barometry, and rock textures that requires differentiation of magmas within the upper crust by crystal–liquid fractionation.

We envision the following petrogenetic scenario.

1. Mafic to intermediate melts are incrementally injected into the middle crust where they differentiate via fractional crystallization to form a mid-crustal magma mush. Some of these pulses reach the upper crust, continue to crystallize at the level of emplacement, and solidify to form intermingled magmatic domains forming the Risco Bayo pluton.
2. Through continued injection of mafic to intermediate magma pulses and further differentiation, the mid-crustal magma reservoir produces felsic melt resembling the parental Huemul granite prior to unmixing.
3. Upon emplacement within the upper crust, the parental granite cools and partially crystallizes, and the interstitial melt reaches the granite minimum.
4. As the parental granitic mush crystallizes, second boiling occurs.
5. The volatile phase streams upward along with melt through confined channels within the crystalline framework of the mush.
6. The volatiles accumulate in bubbles within the overlying crystal-poor melt, which solidifies *in situ*, locally preserving miarolitic cavities in the roof zone of the magma reservoir (e.g. Parmigiani *et al.*, 2016).

Thus, volatile-induced filter pressing and melt extraction generates the three complementary domains of the Huemul pluton, and results in a chemical unmixing effect (Fig. 17; Schaen *et al.*, 2017). This process probably operates in conjunction with horizontal crustal shortening (Garibaldi *et al.*, 2018), which would increase melt extraction efficiency.

The discovery of silicic cumulates with the predicted geochemical and textural signatures of crystal concentration provides a new perspective on the mush model of rhyolite generation within the plutonic realm. Our findings suggest that late Miocene plutonic rocks in the Andes preserve crystal–melt dynamics that heretofore have been inferred nearly universally from volcanic systems and rhyolitic tuffs. The visual identity of rock textures and compositional characterization presented here may help to identify silicic cumulates in other plutons.

ACKNOWLEDGEMENTS

We appreciate the support of Brian Beard and Clark Johnson during the Sr isotope work. We are grateful for constructive reviews by Julien Leuthold and Jake Lowenstern as well as editorial handling by James Beard. We thank Bill Schneider for assistance using newly acquired Oxford Instruments software in the SEM laboratory.

FUNDING

This research was supported by National Science Foundation grants EAR-1411779, EAR-1650232, EAR-16502265, and EAR-1650156; University of Wisconsin–Madison Department of Geoscience gift funds; and a Geological Society of America Graduate Research Grant.

SUPPLEMENTARY DATA

Supplementary data for this paper are available at *Journal of Petrology* online.

REFERENCES

Abbott, R. N. (1978). Peritectic reactions in the system An–Ab–Or–Qz–H_2O. *Canadian Mineralogist* **16**, 245–256.

Andersen, N. L., Jicha, B. R., Singer, B. S. & Hildreth, W. (2017). Incremental heating of Bishop Tuff sanidine reveals preeruptive radiogenic Ar and rapid remobilization from cold storage. *Proceedings of the National Academy of Sciences of the USA* **114**, 12407.

Anderson, A. T., Swihart, G. H., Artioli, G. & Geiger, C. A. (1984). Segregation vesicles, gas filter-pressing, and igneous differentiation. *Journal of Geology* **92**, 55–72.

Anderson, J. L. & Smith, D. R. (1995). The effects of temperature and fO_2 on the Al-in-hornblende barometer. *American Mineralogist* **80**, 549–559.

Annen, C., Blundy, J. D. & Sparks, R. S. J. (2006). The genesis of intermediate and silicic magmas in deep crustal hot zones. *Journal of Petrology* **47**, 505–539.

Bachl, C. A., Miller, C. F., Miller, J. S. & Faulds, J. E. (2001). Construction of a pluton: evidence from an exposed cross section of the Searchlight pluton, Eldorado Mountains, Nevada. *Geological Society of America Bulletin* **113**, 1213–1228.

Bachmann, O. & Bergantz, G. W. (2004). On the origin of crystal-poor rhyolites: extracted from batholithic crystal mushes. *Journal of Petrology* **45**, 1565–1582.

Bachmann, O. & Bergantz, G. W. (2008). Rhyolites and their source mushes across tectonic settings. *Journal of Petrology* **49**, 2277–2285.

Bachmann, O. & Huber, C. (2016). Silicic magma reservoirs in the Earth's crust. *American Mineralogist* **101**, 2377–2404.

Bachmann, O., Dungan, M. A. & Bussy, F. (2005). Insights into shallow magmatic processes in large silicic magma bodies: the trace-element record in the Fish Canyon magma body, Colorado. *Contributions to Mineralogy and Petrology* **149**, 338–349.

Bachmann, O., Miller, C. F. & de Silva, S. L. (2007). The volcanic–plutonic connection as a stage for understanding crustal magmatism. *Journal of Volcanology and Geothermal Research* **167**, 1–23.

Bacon, C. R. (1986). Magmatic inclusions in silicic and intermediate volcanic rocks. *Journal of Geophysical Research* **91**, 6091.

Bacon, C. R. & Druitt, T. H. (1988). Compositional evolution of the zoned calcalkaline magma chamber of Mount Mazama, Crater Lake, Oregon. *Contributions to Mineralogy and Petrology* **98**, 224–256, https://doi.org/10.1007/BF00402114.

Barnes, C. G., Coint, N. & Yoshinobu, A. (2016a). Crystal accumulation in a tilted arc batholith. *American Mineralogist* **101**, 1719–1734.

Barnes, C. G., Memeti, V. & Coint, N. (2016b). Deciphering magmatic processes in calc-alkaline plutons using trace-element zoning in hornblende. *American Mineralogist* **101**, 328–342.

Beane, R. & Wiebe, R. A. (2012). Origin of quartz clusters in Vinalhaven granite and porphyry, coastal Maine. *Contributions to Mineralogy and Petrology* **163**, 1069–1082.

Beard, B. L., Ludois, J. M., Lapen, T. J. & Johnson, C. M. (2013). Pre-4·0 billion year weathering on Mars constrained by Rb–Sr geochronology on meteorite ALH84001. *Earth and Planetary Science Letters* **361**, 173–182.

Bédard, J. H. (1994). A procedure for calculating the equilibrium distribution of trace-elements among the minerals of cumulate rocks, and the concentration of trace-elements in the coexisting liquids. *Chemical Geology* **118**, 143–153.

Bergantz, G. W., Schleicher, J. M. & Burgisser, A. (2015). Open-system dynamics and mixing in magma mushes. *Nature Geoscience* **8**, 793–797.

Bindeman, I. N., Davis, A. M. & Drake, M. J. (1998). Ion microprobe study of plagioclase–basalt partition experiments at natural concentration levels of trace-elements. *Geochimica et Cosmochimica Acta* **62**, 1175–1193.

Blundy, J. & Cashman, K. (2001). Ascent-driven crystallisation of dacite magmas at Mount St Helens, 1980–1986. *Contributions to Mineralogy and Petrology* **140**, 631–650.

Blundy, J. D. & Wood, B. J. (1991). Crystal-chemical controls on the partitioning of Sr and Ba between plagioclase feldspar, silicate melts, and hydrothermal solutions. *Geochimica et Cosmochimica Acta* **55**, 193–209.

Boudreau, A. (2016). Bubble migration in a compacting crystal–liquid mush. *Contributions to Mineralogy and Petrology* **171**, 1–17.

Bowen, N. L. (1928). *The Evolution of the Igneous Rocks*. Princeton, NJ: Princeton University Press, 334 pp.

Brophy, J. G. (1991). Composition gaps, critical crystallinity, and fractional crystallization in orogenic (calc-alkaline) magmatic systems. *Contributions to Mineralogy and Petrology* **109**, 173–182.

Campos, J., Hatzfeld, D., Madariaga, R., Lopez, G., Kausel, E., Zollo, A., Iannacone, G., Fromm, R., Barrientos, S. & Lyon-Caen, H. (2002). A seismological study of the 1835 seismic gap in south–central Chile. *Physics of the Earth and Planetary Interiors* **132**, 177–195.

Charlier, B. L. A., Bachmann, O., Davidson, J. P., Dungan, M. A. & Morgan, D. J. (2007). The upper crustal evolution of a large silicic magma body: evidence from crystal-scale Rb–Sr isotopic heterogeneities in the Fish Canyon magmatic system. Colorado. *Journal of Petrology* **48**, 1875–1894.

Claiborne, L. L., Miller, C. F., Walker, B. A., Wooden, J. L., Mazdab, F. K. & Bea, F. (2006). Tracking magmatic processes through Zr/Hf ratios in rocks and Hf and Ti zoning in zircons: An example from the Spirit Mountain batholith, Nevada. *Mineralogical Magazine* **70**, 517–543.

Coleman, D. S., Gray, W. & Glazner, A. F. (2004). Rethinking the emplacement and evolution of zoned plutons: geochronologic evidence for incremental assembly of the Tuolumne Intrusive Suite, California. *Geology* **32**, 433.

Coleman, D. S., Bartley, J. M., Glazner, A. F. & Pardue, M. J. (2012). Is chemical zonation in plutonic rocks driven by changes in source magma composition or shallow-crustal differentiation? *Geosphere* **8**, 1568–1587.

Collins, W. J., Wiebe, R. A., Healy, B. & Richards, S. W. (2006). Replenishment, crystal accumulation and floor aggradation in the megacrystic Kameruka Suite, Australia. *Journal of Petrology* **47**, 2073–2104.

Cooper, K. M. & Kent, A. J. R. (2014). Rapid remobilization of magmatic crystals kept in cold storage. *Nature* **506**, 480–483.

Cornejo, P. & Mahood, G. (1997). Seeing past the effects of re-equilibration to reconstruct magmatic gradients in plutons: La Gloria Pluton, central Chilean Andes. *Contributions to Mineralogy and Petrology* **127**, 159–175.

Daly, R. A. (1933). *Igneous Rocks and the Depths of the Earth*. New York, NY: McGraw–Hill, 598 pp.

Davidson, J. P., Dungan, M. A., Ferguson, K. M. & Colucci, M. T. (1987). Crust–magma interactions and the evolution of arc magma: the San Pedro–Pellado volcanic complex, southern Chilean Andes. *Geology* **15**, 443–446.

Davidson, J. P., Ferguson, K. M., Colucci, M. T. & Dungan, M. A. (1988). The origin and evolution of magmas from the San Pedro–Pellado volcanic complex, S. Chile: multicomponent sources and open system evolution. *Contributions to Mineralogy and Petrology* **100**, 429–445.

Deckart, K., Godoy, E., Bertens, A., Jerez, D. & Saeed, A. (2010). Barren Miocene granitoids in the Central Andean metallogenic belt, Chile: Geochemistry and Nd–Hf and U–Pb isotope systematics. *Andean Geology* **37**, 1–31.

Deering, C. D. & Bachmann, O. (2010). Trace-element indicators of crystal accumulation in silicic igneous rocks. *Earth and Planetary Science Letters* **297**, 324–331.

Deering, C. D., Keller, B., Schoene, B., Bachmann, O., Beane, R. & Ovtcharova, M. (2016). Zircon record of the plutonic–volcanic connection and protracted rhyolite melt evolution. *Geology* **44**, 267–270.

Donovan, J., Kremser, D., Fournelle, J. & Goemann, K. (2018). *Probe for Windows User's Guide and Reference, Enterprise Edition*. Eugene, OR: Probe Software.

Drake, R. E. (1976). Chronology of Cenozoic igneous and tectonic events in the central Chilean Andes—Latitudes 35°30′ to 36°S. *Journal of Volcanology and Geothermal Research* **1**, 265–284.

Drake, R., Vergara, M., Munizaga, F. & Vicente, J. C. (1982). Geochronology of Mesozoic–Cenozoic magmatism in central Chile, lat. 31°–36°S. *Earth-Science Reviews* **18**, 353–363.

Dufek, J. & Bachmann, O. (2010). Quantum magmatism: magmatic compositional gaps generated by melt–crystal dynamics. *Geology* **38**, 687–690.

Dungan, M. A., Wulff, A., Thompson, R. E. N. & Gene, D. E. (2001). Eruptive stratigraphy of the Tatara–San Pedro complex, 36°S, Southern Volcanic Zone, Chilean Andes: reconstruction method and implications for magma evolution at long-lived arc volcanic centers. *Journal of Petrology* **42**, 555–626.

Ebadi, A. & Johannes, W. (1991). Beginning of melting and composition of first melts in the system Qz–Ab–Or–H_2O–CO_2. *Contributions to Mineralogy and Petrology* **106**, 286–295.

Edmonds, M. & Wallace, P. J. (2017). Volatiles and exsolved vapor in volcanic systems. *Elements* **13**, 29–34.

Fiedrich, A. M., Bachmann, O., Ulmer, P., Deering, C. D., Kunze, K. & Leuthold, J. (2017). Mineralogical, geochemical, and textural indicators of crystal accumulation in the Adamello Batholith (Northern Italy). *American Mineralogist* **102**, 2467–2483.

Garibaldi, N., Tikoff, B., Schaen, A. J. & Singer, B. (2018). Interpreting granitic fabrics in terms of rhyolitic melt segregation, accumulation and escape via tectonic filter pressing in the Huemul pluton, Chile. *Journal of Geophysical Research: Solid Earth*, doi: 10.1029/2018JB016282.

Gelman, S. E., Deering, C. D., Bachmann, O., Huber, C. & Gutiérrez, F. J. (2014). Identifying the crystal graveyards remaining after large silicic eruptions. *Earth and Planetary Science Letters* **403**, 299–306.

Glazner, A. F., Bartley, J. M., Coleman, D. S., Gray, W. & Taylor, R. Z. (2004). Are plutons assembled over millions of years by amalgamation from small magma chambers? *GSA Today* **14**, 4–11.

Glazner, A. F., Coleman, D. S. & Bartley, J. M. (2008). The tenuous connection between high-silica rhyolites and granodiorite plutons. *Geology* **36**, 183–186.

Glazner, A. F., Coleman, D. S. & Mills, R. D. (2015). The volcanic--plutonic connection. In: Breitkreuz, C. & Rocchi, S. (eds) *Physical Geology of Shallow Magmatic Systems: Dykes, Sills and Laccoliths, Advances in Volcanology*, Springer, p. 61–82.

Graeter, K. A., Beane, R. J., Deering, C. D., Gravley, D. & Bachmann, O. (2015). Formation of rhyolite at the Okataina Volcanic Complex, New Zealand: new insights from analysis of quartz clusters in plutonic lithics. *American Mineralogist* **100**, 1778–1789.

Gualda, G. A R. & Ghiorso, M. S. (2013). Low-pressure origin of high-silica rhyolites and granites. *Journal of Geology* **121**, 537–545.

Gualda, G. A. R., Ghiorso, M. S., Lemons, R. V. & Carley, T. L. (2012). Rhyolite-MELTS: a modified calibration of MELTS optimized for silica-rich, fluid-bearing magmatic systems. *Journal of Petrology* **53**, 875–890.

Harper, B. E., Miller, C. F., Koteas, G. C., Cates, N. L., Wiebe, R. A., Lazzareschi, D. S. & Cribb, J. W. (2004). Granites, dynamic magma chamber processes and pluton construction: the Aztec Wash pluton, Eldorado Mountains, Nevada, USA. *Earth and Environmental Science Transactions of the Royal Society of Edinburgh* **95**, 277.

Hawthorne, F., Oberti, R., Harlow, G. E., Maresch, W. V., Martin, R. F., Schumacher, J. C. & Welch, M. D. (2012). Nomenclature of the amphibole supergroup. *American Mineralogist* **97**, 2031–2048.

Heit, B., Yuan, X., Bianchi, M., Sodoudi, F. & Kind, R. (2008). Crustal thickness estimation beneath the southern central Andes at 30°S and 36°S from S wave receiver function analysis. *Geophysical Journal International* **174**, 249–254.

Hildreth, W. (1981). Gradients in silicic magma chambers: implications for lithospheric magmatism. *Journal of Geophysical Research: Solid Earth* **86**, 10153–10192.

Hildreth, W. (2004). Volcanological perspectives on Long Valley, Mammoth Mountain, and Mono Craters: several contiguous but discrete systems. *Journal of Volcanology and Geothermal Research* **136**, 169–198.

Hildreth, W. & Moorbath, S. (1988). Crustal contributions to arc magmatism in the Andes of Central Chile. *Contributions to Mineralogy and Petrology* **98**, 455–489.

Hildreth, W. & Wilson, C. J. N. (2007). Compositional zoning of the Bishop Tuff. *Journal of Petrology* **48**, 951–999.

Hildreth, W., Godoy, E., Fierstein, J. & Singer, B. (2010). Laguna del Maule Volcanic Field, eruptive history of a Quaternary basalt-to-rhyolite distributed volcanic field on the Andean rangecrest in central Chile. *Servicio Nacional de Geologia y Mineria, Boletin* **63**, 145.

Holness, M. B. (2018). Melt segregation from silicic crystal mushes: a critical appraisal of possible mechanisms and their microstructural record. *Contributions to Mineralogy and Petrology* **173**, 48.

Irvine, T. N. (1982). Terminology for layered intrusions. *Journal of Petrology* **23**, 127–162.

Johnson, C. M., Czamanske, G. K. & Lipman, P. W. (1989). Geochemistry of intrusive rocks associated with the Latir volcanic field, New Mexico, and contrasts between evolution of plutonic and volcanic rocks. *Contributions to Mineralogy and Petrology* **103**, 90–109.

Kay, S. M., Godoy, E. & Kurtz, A. (2005). Episodic arc migration, crustal thickening, subduction erosion, and magmatism in the south–central Andes. *Geological Society of America Bulletin* **117**, 67.

Keller, C. B., Schoene, B., Barboni, M., Samperton, K. M. & Husson, J. M. (2015). Volcanic–plutonic parity and the differentiation of the continental crust. *Nature* **523**, 301.

Kurtz, A. C., Kay, S. M., Charrier, R. & Farrar, E. (1997). Geochronology of Miocene plutons and exhumation history of the El Teniente region, Central Chile (34–35°S). *Revista Geologica de Chile* **24**, 75–90

Lee, C. T. A. & Morton, D. M. (2015). High silica granites: terminal porosity and crystal settling in shallow magma chambers. *Earth and Planetary Science Letters* **409**, 23–31.

Leuthold, J., Muntener, O., Baumgartner, L. P. & Putlitz, B. (2014). Petrological constraints on the recycling of mafic crystal mushes and intrusion of braided sills in the Torres del Paine mafic complex (Patagonia). *Journal of Petrology* **55**, 917–949.

Lipman, P. W. (2007). Incremental assembly and prolonged consolidation of Cordilleran magma chambers: evidence from the Southern Rocky Mountain volcanic field. *Geosphere* **3**, 42–70.

Lipman, P. W. & Bachmann, O. (2015). Ignimbrites to batholiths: Integrating perspectives from geological, geophysical, and geochronological data. *Geosphere* **11**, 705–739.

Lucassen, F., Trumbull, R., Franz, G., Creixell, C., Vasquez, P., Romer, R. L. & Figueroa, O. (2004). Distinguishing crustal recycling and juvenile additions at active continental margins: the Paleozoic to recent compositional evolution of the Chilean Pacific margin (36–41°S). *Journal of South American Earth Sciences* **17**, 103–119.

Lundstrom, C. C. & Glazner, A. F. (2016). Silicic magmatism and the volcanic–plutonic connection. *Elements* **12**, 91–96.

Luth, W. C., Jahns, R. H. & Tuttle, O. F. (1964). The granite system at pressures of 4 to 10 kilobars. *Journal of Geophysical Research* **69**, 759–773.

McCaffrey, K. J. & Petford, N. (1997). Are granitic intrusions scale invariant? *Journal of the Geological Society, London* **154**, 1–4.

McKinney, S. T., Cottle, J. M. & Lederer, G. W. (2015). Evaluating rare earth element (REE) mineralization mechanisms in Proterozoic gneiss, Music Valley, California. *Geological Society of America Bulletin* **127**, 1135–1152.

Michel, J., Baumgartner, L., Putlitz, B., Schaltegger, U. & Ovtcharova, M. (2008). Incremental growth of the Patagonian Torres del Paine laccolith over 90 k.y. *Geology* **36**, 459–462.

Miller, C. F. & Miller, J. S. (2002). Contrasting stratified plutons exposed in tilt blocks, Eldorado Mountains, Colorado River Rift, NV, USA. *Lithos* **61**, 209–224.

Miller, C. F., Furbish, D. J., Walker, B. A., Claiborne, L. L., Koteas, G. C., Bleick, H. A. & Miller, J. S. (2011). Growth of plutons by incremental emplacement of sheets in crystal-rich host: Evidence from Miocene intrusions of the Colorado River region, Nevada, USA. *Tectonophysics* **500**, 65–77.

Mills, R. D. & Coleman, D. S. (2013). Temporal and chemical connections between plutons and ignimbrites from the Mount Princeton magmatic center. *Contributions to Mineralogy and Petrology* **165**, 961–980.

Morse, S. A. (1979). Kiglapait geochemistry. 2. Petrography. *Journal of Petrology* **20**, 591–624.

Morse, S. A. (1982). Adcumulus growth of anorthosite at the base of the lunar crust. *Journal of Geophysical Research* **87**, A10–A18.

Muñoz, J., & Niemeyer, H. (1984). Hoja Laguna del Maule, Regiones del Maule y Bío Bío. *Carta Geológica de Chile, Servicio Nacional de Geología Y Minería de Chile, Scale* **64**, 1.

Mutch, E. J. F., Blundy, J. D., Tattitch, B. C., Cooper, F. J. & Brooker, R. A. (2016). An experimental study of amphibole stability in low-pressure granitic magmas and a revised Al-in-hornblende geobarometer. *Contributions to Mineralogy and Petrology* **171**, 1–27.

Nelson, S. T., Davidson, J. P., Heizler, M. T. & Kowallis, B. J. (1999). Tertiary tectonic history of the southern Andes: the subvolcanic sequence to the Tatara–San Pedro volcanic complex, lat 36°S. *Geological Society of America Bulletin* **111**, 1387–1404.

O'Driscoll, B. & VanTongeren, J. A. (2017). Layered intrusions: from petrological paradigms to precious metal repositories. *Elements* **13**, 383–389.

Parada, M. A. (1990). Granitoid plutonism in central Chile and its geodynamic implications; A review. In: Kay, S. M. & Rapela, C. W. (eds) *Plutonism from Antarctica to Alaska: Boulder, Colorado, Geological Society of America Special Paper* **241**, 51–65.

Parmigiani, A., Faroughi, S., Huber, C., Bachmann, O. & Su, Y. (2016). Bubble accumulation and its role in the evolution of magma reservoirs in the upper crust. *Nature* **532**, 492–495.

Paterson, S. R., Vernon, R. H. & Zak, J. (2005). Mechanical instabilities and accumulations of K-feldspar megacrysts in granitic magma, Tuolumne Intrusive Suite, California, USA. *Journal of the Virtual Explorer* **18**, Paper 1.

Petford, N., Cruden, A R., McCaffrey, K. J. & Vigneresse, J. L. (2000). Granite magma formation, transport and emplacement in the Earth's crust. *Nature* **408**, 669–673.

Philpotts, A. R. & Asher, P. M. (1994). Magmatic flow-direction indicators in a giant diabase feeder dike, Connecticut. *Geology* **22**, 363–366.

Rosenberg, C. L. (2001). Deformation of partially molten granite: a review and comparison of experimental and natural case studies. *International Journal of Earth Sciences* **90**, 60–76.

Rubin, A. E., Cooper, K. M., Till, C. B., Kent, A. J. R., Costa, F., Bose, M., Gravley, D., Deering, C. & Cole, J. (2017). Rapid cooling and cold storage in a silicic magma reservoir recorded in individual crystals. *Science* **356**, 1154–1156.

Satkoski, A. M., Fralick, P., Beard, B. L. & Johnson, C. M. (2017). Initiation of modern-style plate tectonics recorded in Mesoarchean marine chemical sediments. *Geochimica et Cosmochimica Acta* **209**, 216–232.

Sawyer, E. W. (2000). Grain-scale and outcrop-scale distribution and movement of melt in a crystallising granite. *Transactions of the Royal Society of Edinburgh: Earth Sciences* **91**, 73–85.

Schaen, A. J., Cottle, J. M., Singer, B. S., Keller, C. B. & Garibaldi, N. (2017). Complementary crystal accumulation and rhyolite melt segregation in a late Miocene Andean pluton. *Geology* **45**, 835–838.

Schöpa, A. & Annen, C. (2013). The effects of magma flux variations on the formation and lifetime of large silicic magma chambers. *Journal of Geophysical Research: Solid Earth* **118**, 926–942.

Shelley, D. M. (1985). Determining paleo-flow directions from ground-mass fabrics in the Lyttleton radial dykes, New Zealand. *Journal of Volcanology and Geothermal Research* **25**, 69–79.

Singer, B. S., Thompson, R. A., Dungan, M. A., Feeley, T. C., Nelson, S. T., Pickens, J. C., Brown, L. L., Wulff, A. W., Davidson, J. P. & Metzger, J. (1997). Volcanism and erosion during the past 930 k.y. at the Tatara–San Pedro complex, Chilean Andes. *Geological Society of America Bulletin* **109**, 127–142.

Singer, B. S., Andersen, N. L., Le Mével, H., Feigl, K. L., DeMets, C., Tikoff, B., Thurber, C. H., Jicha, B. R., Cardona, C., Córdova, L., Gil, F., Unsworth, M. J., Williams-Jones, G., Miller, C., Fierstein, J., Hildreth, W. & Vazquez, J. (2014). Dynamics of a large, restless, rhyolitic magma system at Laguna del Maule, southern Andes, Chile. *GSA Today* **24**, 4–10.

Sisson, T. W. & Bacon, C. R. (1999). Gas-driven filter pressing in magmas. *Geology* **27**, 613–616.

Sparks, R. S. J., Huppert, H. E., Kerr, R. C., McKenzie, D. P. & Tait, S. R. (1985). Postcumulus processes in layered intrusions. *Geological Magazine* **122**, 555.

Statham, P., Penman, C., Chaldecott, J., Burgess, S., Sitzman, S. & Hyde, A. (2013). Validating a new approach to the mapping of phases by EDS by comparison with the results of simultaneous data collection by EBSD. *Microscopy and Microanalysis* **19**, 752–753.

Stern, C. R. & Skewes, M. A. (1995). Miocene to present magmatic evolution at the northern end of the Andean Southern Volcanic Zone, Central Chile. *Revista Geologica de Chile* **22**, 261–272.

Stewart, D. B. & Roseboom, E. H. (1962). Lower temperature terminations of the three-phase region plagioclase–alkali feldspar–liquid. *Journal of Petrology* **3**, 280–315.

Tappa, M. J., Coleman, D. S., Mills, R. D. & Samperton, K. M. (2011). The plutonic record of a silicic ignimbrite from the Latir volcanic field, New Mexico. *Geochemistry, Geophysics, Geosystems* **12**, 1–16.

Tuttle, O. F. & Bowen, N. L. (1958). *Origin of granite in the light of experimental studies in the system NaAlSi3O8–KAlSi3O8–SiO2–H2O. Geological Society of America, Memoirs* **74**, 153 pp.

Vance, J. A. (1969). On synneusis. *Contributions to Mineralogy and Petrology* **24**, 7–29.

Vernon, R. H. (2000). Review of microstructural evidence of magmatic and solid-state flow. *Visual Geosciences* **5**, 1–23.

Vernon, R. H. & Collins, W. J. (2011). Structural criteria for identifying granitic cumulates. *Journal of Geology* **119**, 127–142.

Vernon, R. H. & Paterson, S. R. (2008). Mesoscopic structures resulting from crystal accumulation and melt movement in granites. *Transactions of the Royal Society of Edinburgh: Earth Sciences* **97**, 369–381.

Wager, L. R. (1963). The mechanism of adcumulus growth in the layered series of the Skaergaard intrusion. In: Jerome Fisher, D. Frueh, Jr. A. J. Hurlbut, Jr. C. S. and Tilley, C. E. (eds). *International Mineralogical Association Papers and Proceedings of the Third General Meeting, Washington, D.C., April 17-20, 1962, Monograph* **1**, 1–9.

Wager, L. R. & Brown, G. M. (1968). *Layered Igneous Rocks*. San Francisco, CA: W. H. Freeman, 588 pp.

Wager, L. R., Brown, G. M. & Wadsworth, W. J. (1960). Types of igneous cumulates. *Journal of Petrology* **1**, 73–85.

Wark, D. A., Hildreth, W., Spear, F. S., Cherniak, D. J. & Watson, E. B. (2007). Pre-eruption recharge of the Bishop magma system. *Geology* **35**, 235–238.

Wiebe, R. A. & Collins, W. J. (1998). Depositional features and stratigraphic sections in granitic plutons: Implications for the emplacement and crystallization of granitic magma. *Journal of Structural Geology* **20**, 1273–1289.

Wiebe, R. A., Blair, K. D., Hawkins, D. P. & Sabine, C. P. (2002). Mafic injections, *in situ* hybridization, and crystal accumulation in the Pyramid Peak granite, California. *Geological Society of America Bulletin* **114**, 909–920.

Wiebe, R. A., Wark, D. A. & Hawkins, D. P. (2007). Insights from quartz cathodoluminescence zoning into crystallization of the Vinalhaven granite, coastal Maine. *Contributions to Mineralogy and Petrology* **154**, 439–453.

Yuan, X., Asch, G., Bataille, K., Bock, G., Bohm, M., Echtler, H., Kind, R., Oncken, O. & Wolbern, I. (2006). Deep seismic images of the Southern Andes. In: Kay, S. M. and Ramos, V. A. (eds) *Evolution of an Andean Margin: A Tectonic and Magmatic View from the Andes to the Neuquen Basin (35–29° S Lat). Geological Society of America, Special Papers* **407**, 61–72.